Published in final edited form as:
Neuroimage. 2007 January 1; 34(1): 44–60. doi:10.1016/j.neuroimage.2006.08.030.

3D pattern of brain atrophy in HIV/AIDS visualized using tensor-based morphometry

Ming-Chang Chiang[a], **Rebecca A. Dutton**[a], **Kiralee M. Hayashi**[a], **Oscar L. Lopez**[b], **Howard J. Aizenstein**[c], **Arthur W. Toga**[a], **James T. Becker**[b,c,d], and **Paul M. Thompson**[a,*]

[a]Laboratory of Neuro Imaging, Department of Neurology, UCLA School of Medicine, 635 Charles E. Young Drive South, Suite 225E, Los Angeles, CA 90095-7332, USA

[b]Dept. Neurology, Univ. of Pittsburgh, Pittsburgh, PA 15260, USA

[c]Psychiatry, Univ. of Pittsburgh, Pittsburgh, PA 15260, USA

[d]Psychology, Univ. of Pittsburgh, Pittsburgh, PA 15260, USA

Abstract

35% of HIV-infected patients have cognitive impairment, but the profile of HIV-induced brain damage is still not well understood. Here we used tensor-based morphometry (TBM) to visualize brain deficits and clinical/anatomical correlations in HIV/AIDS. To perform TBM, we developed a new MRI-based analysis technique that uses fluid image warping, and a new α-entropy-based information-theoretic measure of image correspondence, called the Jensen–Rényi divergence (JRD).

Methods—3D T1-weighted brain MRIs of 26 AIDS patients (CDC stage C and/or 3 without HIV-associated dementia; 47.2 ± 9.8 years; 25M/1F; $CD4^+$ T-cell count: 299.5 ± 175.7/μl; $\log_{10}$ plasma viral load: 2.57 ± 1.28 RNA copies/ml) and 14 HIV-seronegative controls (37.6 ± 12.2 years; 8M/6F) were fluidly registered by applying forces throughout each deforming image to maximize the JRD between it and a target image (from a control subject). The 3D fluid registration was regularized using the linearized Cauchy–Navier operator. Fine-scale volumetric differences between diagnostic groups were mapped. Regions were identified where brain atrophy correlated with clinical measures.

Results—Severe atrophy (~15–20% deficit) was detected bilaterally in the primary and association sensorimotor areas. Atrophy of these regions, particularly in the white matter, correlated with cognitive impairment (P=0.033) and $CD4^+$ T-lymphocyte depletion (P=0.005).

Conclusion—TBM facilitates 3D visualization of AIDS neuropathology in living patients scanned with MRI. Severe atrophy in frontoparietal and striatal areas may underlie early cognitive dysfunction in AIDS patients, and may signal the imminent onset of AIDS dementia complex.

Introduction

The hallmark of acquired immune deficiency syndrome (AIDS)/human immunodeficiency virus (HIV) infection is progressive immunosuppression, particularly the depletion of $CD4^+$ T-lymphocytes. HIV enters the brain within 2 weeks of initial infection (Paul et al., 2002), and damages neurons primarily by stimulating the production of cytokines that are toxic to neurons, leading to excitotoxic cell death. Thirty-five percent of HIV-infected patients have some signs of neurocognitive dysfunction (White et al., 1995), characterized by difficulties

*Corresponding author. Fax: +1 310 206 5518. thompson@loni.ucla.edu (P.M. Thompson).

in concentration, psychomotor slowing, and impaired information processing (Becker et al., 1997). In the more advanced stages of the disease, around 15% of AIDS patients have HIV-associated dementia, a complex disorder consisting of psychomotor slowing, behavioral abnormalities, and Parkinsonian features such as bradykinesia and gait disturbance (McArthur et al., 2005). Decline in neurocognitive function predicts and directly contributes to mortality (Sacktor et al., 1996).

HIV encephalopathy is pathologically characterized by diffuse white matter pallor and rarefaction, as well as astrocytic cell death. The blood–brain barrier breaks down and HIV-induced cytokines and neurotoxins are produced, causing dendritic simplification and neuronal loss. Regionally, central white matter and deep gray matter structures – such as the basal ganglia, thalamus, and brainstem – are particularly vulnerable to atrophy (Budka et al., 1987; Price et al., 1988; Thompson et al., 2001; Gray et al., 2003; Bell, 2004; McArthur et al., 2005). In a recent MRI study, we found selective cortical thinning in primary sensorimotor, premotor, and visual areas in AIDS (Thompson et al., 2005). Surface-based anatomical maps also revealed regional atrophy in the caudate and hippocampus (Becker et al., submitted for publication-a) as well as corpus callosum thinning and ventricular expansion (Thompson et al., 2006). However, there is a still a lack of detailed 3D maps that show the profile of HIV-associated changes throughout the brain. More conventional volumetric studies were the first to demonstrate global white matter atrophy, basal ganglia volume loss, and ventricular enlargement (Aylward et al., 1993; Hall et al., 1996; Stout et al., 1998). Nevertheless, volumetric studies are generally labor-intensive and cannot visualize the profile of deficits at the voxel level. Other imaging modalities, such as magnetic resonance spectroscopy (MRS; Chang et al., 1999) or diffusion tensor imaging (DTI; Filippi et al., 2001), reveal early white matter abnormalities that are not visible on structural MRI, but they suffer from limited spatial resolution.

Here we applied tensor-based morphometry (TBM; see Davatzikos et al., 1996; 2001; Thompson et al., 2000; Chung et al., 2001, 2003, 2004; Fox et al., 2001; Shen and Davatzikos, 2003; Studholme et al., 2001, 2003, 2004; Teipel et al., 2004, for related work) to detect and automatically quantify the subtle and distributed patterns of brain atrophy in HIV/AIDS.

TBM and image deformation approach

In a cross-sectional TBM design the most important step in the morphometric analysis is to nonlinearly deform all the images to match a preselected brain image, which acts as a template. Then, the Jacobian determinant (i.e., the local expansion factor) of the deformation fields is used to gauge the local volume differences between the individual images and the template, and these can be analyzed statistically to identify group differences or localized atrophy at the voxel level. Automated image registration, which aligns one image with another, is typically guided by quantitative measures of image similarity based on the statistical dependence of the voxel intensities, such as their correlation (Collins et al., 1994), summed squared intensity differences (Woods et al., 1998; Ashburner and Friston, 1999), or more complex measures derived from the joint histogram of the registered images, such as ratio image uniformity (Woods et al., 1992). Among these different approaches, the mutual information method (MI; Viola and Wells, 1997) has proved popular and highly effective, and assumes that MI of two images is maximal when the images are optimally aligned. The parameters of the alignment transformation are tuned to maximize the MI. The MI method has been successfully applied to rigid (Viola and Wells, 1997), non-rigid (Lorenzen et al., 2004; Studholme et al., 2001), and cross-modality registrations (e.g., MRI to PET or histologic images; Kim et al., 1997). Hermosillo (2002) developed a variational formulation to maximize MI using a regularization functional borrowed from linear elasticity theory. This was further extended (D'Agostino et al., 2003) to deal with large local deformations

while maintaining one-to-one topology (Christensen et al., 1996) using a viscous fluid model. Related work on diffeomorphic matching techniques can be found in Miller (2004), and Avants and Gee (2004); these registration methods can handle large deformations without disrupting the image topology.

He et al. (2003) were the first to apply the Jensen–Rényi divergence (JRD) to image registration. The concept of MI was generalized in an information-theoretic framework derived from Rényi's α-entropy that allows an extra degree of freedom (α) in which MI α=1 is a special case. They showed that the JRD was more robust than MI for 2D inverse synthetic aperture radar (ISAR) image registrations involving translations, rotations and scaling.

In this paper, we modify the original definition of JRD to drive nonlinear image registration. JRD has been applied before to rigid registration by Pluim et al. (2004) but the nonlinear case has not been studied. We iteratively determine the driving force at each voxel such that the JRD between the deforming source and target images is maximized under the viscous fluid regularization (Christensen et al., 1996). This means that the transforms have the important property of being smooth (i.e., continuous and differentiable) as well as one-to-one – there can be no tearing or folding of the image – as the permissible transformations are constrained to obey the constitutive laws of a compressible fluid, as defined rigorously in the framework of continuum mechanics. In this paper, we first show that our algorithm performs well on 2D and 3D images with different noise and intensity distributions. We then apply the JRD algorithm to a neuroscientific study using TBM, and mapping the profile of brain atrophy in HIV/AIDS. We show that this atrophy is selective and associated, in specific brain regions, with decline in cellular immunity and neurocognitive deterioration, providing a valuable biological measure of the disease process.

Methods

Jensen–Rényi divergence

If $\boldsymbol{I} \in \boldsymbol{R}$ is a continuous random variable with probability density function $p(i)$, the Rényi α-entropy is defined as (Principe and Xu, 1999)

$$\boldsymbol{R}_\alpha(\boldsymbol{I})=\boldsymbol{R}_\alpha(p(i))=\frac{1}{1-\alpha}\log\left(\int_R p(i)^\alpha di\right), \alpha>0 \text{ and } \alpha \neq 1. \quad (1)$$

Here we restrict 0<α<1 to keep the Rényi α-entropy concave (Hamza and Krim, 2003; He et al., 2003).

Let $\boldsymbol{I}_1$ and $\boldsymbol{I}_2$ be the target and the deforming source images respectively, and $\boldsymbol{I}_1, \boldsymbol{I}_2$: $\boldsymbol{R}^d \rightarrow \boldsymbol{R}$, d=1, 2, or 3. Let $\Omega \subseteq \boldsymbol{R}^d$ be the region of overlap of both images with volume V and $\mathbf{u}$ a deformation vector field in Ω. We modified the definition of JRD for registration of two images (Hamza and Krim, 2003; He et al., 2003), which is based on the conditional intensity distribution of the transformed image given the target image, by extending the definition from discrete random variables to continuous variables, such that the JRD (denoted $D_\alpha(\mathbf{u})$) of voxel intensities between $\boldsymbol{I}_1(\mathbf{x})$ and $\boldsymbol{I}_2(\mathbf{x}-\mathbf{u})$, with respect to $\mathbf{u}$, is given by

$$
\begin{aligned}
D_\alpha(\mathbf{u}) = & \boldsymbol{R}_\alpha \left(\int_R w(i_1) p_u(i_2|i_1) di_1 \right) \\
& - \int_R w(i_1) \boldsymbol{R}_\alpha (\mathbf{I}_2|\mathbf{I}_1) di_1 \\
= & \frac{1}{1-\alpha} \log \lfloor \int_R \left(\int_R w(i_1) p_u(i_2|i_1) di_1 \right)^\alpha di_2 \rfloor \\
& - \int_R w(i_1) \left(\frac{1}{1-\alpha} \log \left(\int_R p_{\mathbf{u}}(i_2|i_1)^\alpha di_2 \right) \right) di_1,
\end{aligned} \tag{2}
$$

where $p_u(i_2|i_1) = \frac{p_u(i_1, i_2)}{p(i_1)}$ is the conditional density function of $\boldsymbol{I}_2(\mathbf{x}-\mathbf{u})$ given $\boldsymbol{I}_1(\mathbf{x})$; $p_u(i_1, i_2)$ and $p(i_1)$ are joint and marginal density functions respectively. $w(i_1)$is a weight function.

If we set $w(i_1)=p(i_1)$, with $p_u(i_2)=\int_R p_u(i_1, i_2)\, di_1$, the JRD becomes (see Appendix A for details)

$$
D_\alpha(\mathbf{u}) = \frac{1}{1-\alpha} \left\{ \log \left(\int_R p_u(i_2)^\alpha di_2 \right) - \int_R p(i_1) \log \left(\int_R p_u(i_1, i_2)^\alpha di_2 \right) di_1 + \alpha \int_R p(i_1) \log p(i_1) di_1 \right\}. \tag{3}
$$

When $\alpha \to 1$, this expression for the JRD yields

$$
D_1(\mathbf{u}) = \int_{R^2} p_u(i_1, i_2) \log \frac{p_u(i_1, i_2)}{p(i_1) p_u(i_2)} di_1 di_2, \tag{4}
$$

which is exactly the formula for the mutual information as in Hermosillo (2002), and D'Agostino et al. (2003).

We followed the method of Christensen et al. (1996), where the deforming template image was treated as embedded in a compressible viscous fluid governed by the Navier–Stokes equation for conservation of momentum, simplified to a linear PDE:

$$
\mathbf{L}\mathbf{v} = \mu \nabla^2 \mathbf{v} + (\lambda + \mu) \nabla (\nabla \cdot \mathbf{v}) = \mathbf{F}(\mathbf{x}, \mathbf{u}). \tag{5}
$$

Here **v** is the deformation velocity, and μ and λ are the viscosity constants.

We adopted variational calculus methods (Hermosillo, 2002; D'Agostino et al., 2003) to define a force field $\mathbf{F}(\mathbf{x}, \mathbf{u})$ throughout the deforming image, such that $D_\alpha(\mathbf{u})$ is maximized, and used $\tilde{D}_\alpha(\mathbf{u}) = -D_\alpha(\mathbf{u})$ to transform a maximization problem into a minimization. If **w** is a small perturbation of **u**, taking the definition of the first variation of $\tilde{D}_\alpha(\mathbf{u})$ and Eq. (3) together, with $\frac{\partial p_{\mathbf{u}+\varepsilon\mathbf{w}}(i_2)}{\partial \varepsilon} = \int_R \frac{\partial p_{\mathbf{u}+\varepsilon\mathbf{w}}(i_1, i_2)}{\partial \varepsilon} di_1$, we have (see Appendix B for details)

$$\left.\frac{\partial \tilde{D}_\alpha(\mathbf{u}+\varepsilon\mathbf{w})}{\partial\varepsilon}\right|_{\varepsilon=0} = \frac{-\alpha}{1-\alpha}\int_{R^2}\left[\frac{p_{\mathbf{u}+\varepsilon\mathbf{w}}(i_2)^{\alpha-1}}{k_{\mathbf{u}+\varepsilon\mathbf{w},\alpha}} - \frac{p(i_1)p_{\mathbf{u}+\varepsilon\mathbf{w}}(i_1,i_2)^{\alpha-1}}{q_{\mathbf{u}+\varepsilon\mathbf{w},\alpha}(i_1)}\right]\left.\frac{\partial p_{u+\varepsilon\mathbf{w}}(i_1,i_2)}{\partial\varepsilon}\right|_{\varepsilon=0} di_1 di_2, \quad (6)$$

where $k_{\mathbf{u}+\varepsilon\mathbf{w},\alpha}=\int_R p_{\mathbf{u}+\varepsilon\mathbf{w}}(i_2)^\alpha\, di_2$, and $q_{\mathbf{u}+\varepsilon\mathbf{w},\alpha}(i_1)=\int_R p_{\mathbf{u}+\varepsilon\mathbf{w}}(i_1,i_2)^\alpha\, di_2$.

The joint probability density function $p_{\mathbf{u}}(i_1, i_2)$, of the registered images, was estimated by the Parzen window method (Hermosillo, 2002). We chose a Gaussian function with variance h^2 as the Parzen kernel:

$$p_{\mathbf{u}}(i_1,i_2)=\frac{1}{V}\int_\Omega \psi_h(i_1-\mathbf{I}_1(\mathbf{x}), i_2-\mathbf{I}_2(\mathbf{x}-\mathbf{u}))d\mathbf{x}, \quad (7)$$

where $\psi_h(i_1,i_2)=(\sqrt{2\pi}h)^{-2}\cdot\exp\left[-(i_1^2+i_2^2)/2h^2\right]$.

Inserting Eq. (7) into (6) and rearranging as in Hermosillo (2002), and D'Agostino et al. (2003), gives

$$\left.\frac{\partial \tilde{D}_\alpha(\mathbf{u}+\varepsilon\mathbf{w})}{\partial\varepsilon}\right|_{\varepsilon=0} = \frac{\alpha}{1-\alpha}\frac{1}{V}\int_\Omega\left[L_{\mathbf{u},\alpha}(i_1,i_2)^*\frac{\partial\psi_h}{\partial i_2}\right](\mathbf{I}_1(\mathbf{x}),\mathbf{I}_2(\mathbf{x}-\mathbf{u}))\nabla\mathbf{I}_2(\mathbf{x}-\mathbf{u})\mathbf{w}(\mathbf{x})d\mathbf{x}, \quad (8)$$

where $\mathbf{L}_{\mathbf{u},\alpha}(i_1,i_2)=\frac{p_{\mathbf{u}}(i_2)^{\alpha-1}}{k_{\mathbf{u},\alpha}} - \frac{p(i_1)p_{\mathbf{u}}(i_1,i_2)^{\alpha-1}}{q_{u,\alpha}(i_1)}$, and "*" denotes convolution. Therefore, the force field is defined as $\mathbf{F}(\mathbf{x},\mathbf{u})=-\nabla_{\mathbf{u}}D_\alpha$. Taken together with Eq. (8)

$$\mathbf{F}(\mathbf{x},\mathbf{u})=-\frac{\alpha}{1-\alpha}\frac{1}{V}\left[L_{u,\alpha}(i_1,i_2)^*\frac{\partial\psi_h}{\partial i_2}\right](\mathbf{I}_1(\mathbf{x}),\mathbf{I}_2(\mathbf{x}-\mathbf{u}))\nabla I_2(\mathbf{x}-\mathbf{u}). \quad (9)$$

Image registration and tensor-based morphometry

Subject selection and evaluation—Twenty-six AIDS patients (age: 47.2±9.8 years; 25M/1F; $CD4^+$ T-cell count: 299.5±175.7 per μl; $\log_{10}$ viral load: 2.57±1.28 RNA copies per ml of blood plasma) and 14 HIV-seronegative controls (age: 37.6±12.2 years; 8M/6F) underwent MRI scanning; subjects and scans were exactly the same as those analyzed in our cortical thickness study (Thompson et al., 2005), where more detailed neuropsychiatric data from the subjects are presented. All patients met Center for Disease Control criteria for AIDS, stage C and/or 3 (Center for Disease Control and Prevention, 1992), and none had HIV-associated dementia. Health care providers in Allegheny County, PA, served as a sentinel network for recruitment. All AIDS patients were eligible to participate, but those with a history of recent traumatic brain injury, CNS opportunistic infections, lymphoma, or stroke were excluded.

All patients underwent a detailed neurobehavioral assessment within the 4 weeks before their MRI scan, involving a neurological examination, psychosocial interview, and neuropsychological testing, and were designated as having no, mild, or moderate (coded as 0, 1, and 2 respectively) neuropsychological impairment based on a factor analysis of a broad inventory of motor and cognitive tests performed by a neuropsychologist (J.T.B.; see Thompson et al., 2005, for details).

Image acquisition and registration—All subjects received 3D spoiled gradient recovery (SPGR) anatomical brain MRI scans (256 × 256 × 124 matrix, TR=25 ms, TE=5 ms; 24-cm field of view; 1.5-mm slices, zero gap; flip angle=40°) as part of a comprehensive neurobehavioral evaluation. The MRI brain scan of each subject was co-registered with scaling (9-parameter transformation) to the ICBM53 average brain template (Mazziotta et al., 2001), after removal of extracerebral tissues (e.g., scalp, meninges, brainstem and cerebellum). The template is one of several standardized adult brain templates in the ICBM standard space and was generated using the nonlinear image registration tool ANIMAL (Collins et al., 1995) by Louis Collins (Montreal Neurological Institute, McGill University, Canada), and is part of the MINC distribution of brain templates, image analysis algorithms and display software. To save computation time and memory requirements, the source and the target images were filtered with a Hann-windowed sinc kernel, isotropically downsampled by a factor of 2, and registered to a randomly selected control subject's image by maximizing the JRD. As in other TBM studies, e.g., Studholme et al., 2001; Davatzikos et al., 2001, we preferred registration to a typical control image versus a multi-subject average intensity atlas as it had sharper features and, in general, larger effect sizes, as shown in Fig. 1; nevertheless, template optimization for TBM is the subject of further on-going study by us and others (Kochunov et al., 2002, 2005; Avants and Gee, 2004; Fletcher et al., 2004; Studholme and Cardenas, 2004; Twining et al., 2005). The α value of JRD was set to 0.95 (see below for the selection of α), and the Parzen parameter h was determined by the pseudo-likelihood method (D'Agostino et al., 2003). On solving Eq. (5), μ and λ are set to 0.9 and 6.0 in all of the following experiments. A relatively high setting for λ is useful to penalize extreme volume distortions in the deforming template, and to keep any such distortions spatially smooth. The velocity field $\mathbf{v}$ was computed iteratively by convolving the force field with a filter kernel of size D, which is the Green's function represented in terms of the eigenfunctions of the linear operator $\boldsymbol{L}$ (Bro-Nielsen and Gramkow, 1996). A Fast Fourier transform was used to perform this computationally expensive convolution. The deformation was obtained from $\mathbf{v}$ by Euler integration over time, and the deformed template image was regridded when the Jacobian determinant of the deformation mapping at any point in $\mathbf{x}-\mathbf{u}$ was smaller than 0.5. We refer readers to Christensen et al. (1996), for details. Convergence was declared when JRD was no longer monotonically increasing, up to a maximum of 350 iterations. In the 3D MRI experiments, convergence was usually achieved by around 50 to 70 iterations, making the setting of 350 iterations a reasonable upper limit. Computation time (for the downsampled images) is about 12 min on SUN Microsystem workstations with a dual 64-bit AMD Opteron 2.4 GHz processor. The resulting deformation field was trilinearly interpolated to drive the source image towards the target at the original resolution to obtain the warped image. The Jacobian determinant of the deformation field was used as a local index of tissue expansion (Jacobian >1) or shrinkage (Jacobian <1) relative to the target (Davatzikos et al., 1996; Chung et al., 2001). The percentage of tissue deficit at each voxel was estimated from the ratio of mean Jacobian determinant of the AIDS to control subjects. This indicates the degree to which the volume of a specific region is lower in AIDS than in matched controls, and the ratio can be turned into a percentage deficit.

Registration performance and selection of α—By contrast with the more conventional MI method, the JRD registration method is more general and has a free parameter, α, that can be optimized (MI corresponds to the special case when α has the value of 1). Following prior work, we employed example geometric shapes used commonly in the image registration literature (2D circles and "C" shapes, that are difficult or impossible to match using so-called "small deformation" registration approaches; see Christensen et al., 1996, for details). Fig. 2 shows how a 2D 256 × 256 image of a circle can be registered to a "C" shape, with accurate boundary correspondences, by maximizing the JRD. Although this

example is not designed to represent the deformation magnitude or image contrast in a real case, the grids confirm that very large deformation of the source image is allowed by viscous fluid regularization (as in Christensen et al., 1996). These fields were confirmed to be non-singular (i.e., no folding; Jacobian positive everywhere). Although the matching here could be realized by an infinite number of possible matching fields, and by cost functions other than JRD, the experiment shows that large deformations are within the "capture range" of the algorithm, and boundary correspondences are correctly achieved. With the same parameters, our method yielded excellent registration accuracy in images consisting of only black and white pixels (i.e., four nonzero points in the joint histogram), with multiple gray levels, and in the presence of noise.

Since the registration of the above two-dimensional shapes, with very simple intensity distributions, may be insufficient to give meaningful information concerning the registration of MR images of the brain, we compared different α values for registration of 3D MR images in terms of the volume of mismatch as well as the effect sizes obtained when detecting group differences. We followed the method proposed by Freeborough et al. (1996) to compute the volume of mismatch between the registered source and target brain MR images. If $i_S(\mathbf{x})$ and $i_T(\mathbf{x})$ are respectively the intensities of the source and the target images, and m_S and m_T are the mean intensities, the volume of mismatch (V_m) between the registered source and target images is given by

$$V_m = \#\left\{ [\mathbf{x} \in \text{Source or } \mathbf{x} \in \text{Target}] \text{ and } \left[\left| \frac{i_s(\mathbf{x})}{m_S} - \frac{i_T(\mathbf{x})}{m_T} \right| > 0.2 \right] \right\}. \quad (10)$$

We compared the registration accuracy based on JRD at different α values and a more standard cost function, the sum of the squared intensity differences (SSD, Woods et al., 1998), in terms of the volume of mismatch. To make sure the SSD cost function is fairly compared to the others, in the case of SSD, prior to image deformation, intensities in the two images were scaled (i.e., intensity normalized) such that the mean intensities over the brain were the same. Fig. 3 shows that the registration accuracy depends on α, and α=0.95 gives minimum volume of mismatch. 3D image registration using JRD is more accurate than using SSD (even after intensity is normalized). Fig. 4 shows the cumulative histograms of the probability maps based on the voxelwise differences of the mean log (Jacobian) between AIDS and control subjects, using the Mann–Whitney *U* test. α=0.95 has greater statistical power in detecting the disease effects than other α values, at least on this dataset. The performance of a large α (α≥0.9) in the 3D experiment is much better than that of SSD. This is natural as the intensity distributions in real MR images are more complex than assumed by SSD.

To demonstrate 3D mapping when α=0.95, different sections of the source, deformed source and the target brain images are shown in Fig. 5 (with the corresponding 3D deformation field shown in Fig. 6). Fig. 7 displays the source brain surfaces, before and after they are deformed to match the target brains in several subjects. The shapes of the gyri, corpus callosum, and ventricles are well matched.

Statistical mapping—The Jacobian determinant values were first subjected to a log transformation because the null distribution of the log(Jacobian) is closer to Normal than that of the Jacobian determinant, which is skewed and bounded below by zero (Ashburner and Friston, 2000; Woods, 2003; Avants et al., 2006; Arsigny et al., 2005; see Leow et al., 2005, 2006, for a detailed analysis of the effects of log-transformation on the Jacobian distribution). We tested the significance of difference between the mean log(Jacobian) of the AIDS and control group using Mann–Whitney *U* test voxelwise. Since women were

outnumbered by men in the AIDS sample but not among the controls (25 men to 1 woman in AIDS, and 8 men to 6 women in controls), we compared the group differences in male subjects only (mean age of male AIDS patients: 47.04±10.21 years, male controls: 42.29±12.80 years, P=0.31) for better control of the age and gender covariates. Spearman's rank test was applied at each voxel to identify regions where brain tissue atrophy in all of the AIDS patients correlated with clinical parameters (e.g., severity of cognitive impairment, $CD4^+$ T-cell count, and plasma viral load; see Results for other parameters tested). We used color-coded maps to visualize uncorrected P values derived from Mann–Whitney U tests or correlation tests. Overall significance was assessed by permutation methods (Nichols and Holmes, 2001) to correct for multiple comparisons. Statistical testing was performed on each random permutation of subjects' labels (e.g., "disease" or "control" in Mann–Whitney U tests, or impairment severity in the correlation test) to construct a null distribution for the number of voxels more significant than a fixed primary threshold applied at the voxel level (here set to p=0.01). The omnibus probability (i.e., corrected for multiple comparisons) was determined by comparing the number of suprathreshold voxels in the true labeling to the permutation distribution. The number of permutations N was chosen to control the standard error SE_p of omnibus probability p, which follows a binomial distribution B(N, p) with $SE_p = \sqrt{p(1-p)/N}$ (Edgington, 1995). We selected N=8000 tests out of the total number of possible permutations ($\approx 8 \times 10^9$) such that the approximate margin of error (95% confidence interval) for p was around 5% of p, and 0.05 was chosen as the significance level.

For stronger control over the likelihood of false rejections of the null hypotheses with multiple comparisons, we adopted the method by Storey (2002), which directly measures the positive false discovery rate (pFDR) under a given primary threshold. The pFDR method is more powerful than the popular sequential P value FDR method (Benjamini and Hochberg, 1995; Genovese et al., 2002), and the pFDR measure is theoretically more suitable for representing the "rate at which discoveries are false" than the FDR measure when the primary rejection region is relatively small (Storey, 2002). Briefly, pFDR is the false discovery rate conditioning on the event that positive findings, rejecting the null hypothesis, have occurred, and is given by

$$\mathrm{pFDR}(\gamma) = \frac{\pi_0 \Pr(P \le \gamma | H=0)}{\Pr(P \le \gamma)} = \frac{\pi_0 \gamma}{\Pr(P \le \gamma)}, \tag{11}$$

where $\pi_0 = Pr(H=0)$ is the probability that the null hypothesis is true, and γ is the rejection threshold for the individual hypothesis (similar to the primary threshold in the permutation tests above), which was set to 0.01 in our experiments. For m hypothesis tests and some well-chosen λ, a conservative estimate of π_0 is given by

$$\widehat{\pi}_0(\lambda) = \frac{\#\{p_i > \lambda\}}{(1-\lambda)m} = \frac{W(\lambda)}{(1-\lambda)m}. \tag{12}$$

Therefore, the estimate of pFDR is

$$p\widehat{\mathrm{FDR}}_\lambda(\gamma) = \frac{\widehat{\pi}_0(\lambda)\gamma}{\widehat{\Pr}(P \le \gamma)} = \frac{W(\lambda)\gamma}{(1-\lambda)R(\gamma)}. \tag{13}$$

Here $\widehat{\Pr}(p \le \gamma)=\frac{\#\{p_i \le \gamma\}}{m}=\frac{R(\gamma)}{m}$. We followed the procedures given in (Storey and Tibshirani, 2001; Storey, 2002) to estimate λ for the pFDR-corrected overall significance value for the statistical maps that were significant under the permutation tests. Briefly, we initially set a range of values for λ, say $\Lambda=\{0, 0.01, 0.02,\ldots, 0.99\}$. For each $\lambda \in \Lambda$, we formed B bootstrap versions $p\,\overline{\mathrm{FDR}}_{\lambda}^{*b}(\gamma)$ of the estimate, $b=1,\ldots, B$, and the mean-squared error of the estimation is given by

$$\overline{\mathrm{MSE}}(\lambda)=\frac{1}{B}\sum_{b=1}^{B}\left[p\,\overline{\mathrm{FDR}}_{\lambda}^{*b}(\gamma)-\min_{\lambda'\in\Lambda} p\,\overline{\mathrm{FDR}}_{\lambda'}(\gamma)\right]^2. \tag{14}$$

Therefore, the best λ was chosen as $\lambda=\mathrm{argmin}_{\lambda\in\Lambda}\,\overline{\mathrm{MSE}}(\lambda)$.

Strictly speaking, although both permutation testing and pFDR methods are both valid, the estimation of pFDR should be considered as an exploratory post hoc test, as permutation testing was planned in advance for inference. Disease effects and clinical correlations in AIDS were somewhat consistently detected with different statistical methods for multiple comparisons correction. In some cases a borderline effect was better detected using permutation testing, but in many cases the corrected significance values were very similar for pFDR.

To assess the significance of the detected group differences and correlations with clinical and neuropsychological measures in the AIDS patients, permutation tests and pFDR measures (Storey, 2002) were performed on gray and white matter separately, to generate *P* values that were corrected for multiple comparisons. White matter and gray matter masks were automatically segmented using an unsupervised Gaussian mixture classifier, after adjusting for spatial intensity inhomogeneity, using the software package “BrainSuite” (Shattuck and Leahy, 2002).

Results

Fig. 8 shows the selective pattern of brain deficits in the HIV/AIDS group (this comparison was performed in male subjects only). We detected 10%–15% brain tissue atrophy (in the white matter mask, permutation test $P=0.018$, pFDR=0.042; not significant in the gray matter mask, permutation test $P=0.058$, pFDR=0.099) bilaterally in the subcortical gray matter (putamen, globus pallidus, and thalamus, which are included in the white matter mask), medial and basal frontal lobes, and specific white matter tracts (corpus callosum, cingulum, and the posterior limb of the internal capsule). Brain atrophy was most severe (~15%–20% loss) in primary and association sensorimotor areas. The temporal lobes were relatively spared. Other slices of the data in Fig. 8 are shown in animation format at the following URL: http://www.loni.ucla.edu/~thompson/HIV/MOVIE/AIDS.html. There was no detected global difference in the total brain volume between AIDS patients and controls (AIDS, 1035.5±100.5 cm^3; controls, 1000.1±55.0 cm^3; $P=0.2$), and no difference when total brain volumes were compared between patients and controls in male subjects only (AIDS, 1043.5±93.8 cm^3; controls, 1013.5±58.4 cm^3; $P=0.4$).

We applied correlation tests within the AIDS group to detect regions in which the degree of atrophy was related to clinical parameters. Brain tissue loss was linked with neuropsychological impairment (in the white matter, the permutation-corrected $P=0.033$, and pFDR=0.045; and, irrespective of the method used for multiple comparisons correction, no correlation was found between atrophy and cognitive impairment in the gray matter:

permutation-corrected P=0.182, and pFDR=0.243; Fig. 9, upper row). Correlations were also observed in medial and basal frontal lobes, genu of corpus callosum, middle part of the cingulate gyrus, and primary and association sensorimotor areas. These regions, along with putamen and globus pallidus, were also associated with decline in $CD4^+$ T-cell numbers (in the white matter, this correlation was detected regardless of the method used for multiple comparisons correction: permutation-corrected P=0.005, and pFDR=0.018; in the gray matter mask, the significance of this correlation was at the borderline significant or trend level, with permutation tests giving P=0.043 and pFDR=0.080; Fig. 9, lower row). There was no correlation of plasma HIV viral load with atrophy in any brain region (P=0.2 in both gray and white matter; maps not shown).

Medication effects

Thirteen of the 26 AIDS subjects were receiving highly active antiretroviral therapy (HAART), an aggressive treatment combining protease and reverse transcriptase inhibitors, designed to reduce viral load and bolster T-cell immunity. We did not detect significant differences in the degree of brain atrophy between patients receiving or not receiving HAART (P=0.5 in both gray and white matter; maps not shown). This may suggest that HAART has no substantial effect on brain morphology, or none at all, but this still needs to be verified in a larger sample, ideally in a longitudinal, randomized study.

Duration of infection

AIDS patients who have been infected longer typically have lower $CD4^+$ T-cell counts (Thompson et al., 2005), so we expected greater magnitude and extent of atrophy as AIDS progresses. However, as in our cortex study (Thompson et al., 2005), we could not detect any such linkage with the estimated duration of infection ($P > 0.1$ in both gray and white matter; maps not shown). This may be ascribed to the inevitable inaccuracies in estimating the duration of infection (based on patients' estimates, successive antibody tests, or inference from specific life events), as there is no reliable index to define the onset of HIV infection. Longitudinal patient scanning is needed to better define the relationship between duration of infection and brain atrophy (Stout et al., 1998).

Age

We regressed age against the Jacobian maps separately in AIDS and in healthy subjects to estimate the profile of age-dependent brain changes. Normal subjects' brains decreased in volume over time in the *genu* of the corpus callosum, posterior limbs of the internal capsule, and lateral temporal and anterior frontal lobes (white matter, permutation test P=0.027, pFDR=0.040; in gray matter, permutation test P=0.05, pFDR=0.057; Fig. 10). This association was only at trend level or not detected in the AIDS group (white matter, P=0.08; gray matter, P=0.27, permutation test; maps not shown), but there was insufficient power to determine whether there was an age × disease interaction.

Discussion

Our study reveals that even before the development of AIDS dementia complex or CNS opportunistic infections, severe brain tissue loss occurs in the striatum, cingulate and callosal fibers, and pericentral regions mediating primary and association sensorimotor functions. Atrophy in these areas is also associated with neuropsychological impairment and depletion of $CD4^+$ T-lymphocytes, indicating that selective brain atrophy accompanies immunosuppression by HIV and may signal the imminent development of AIDS dementia. Although we established the group volumetric differences in men only, we have no reason to believe that the results would not apply to the whole sample of subjects, as there has been no reported difference in disease progression between HIV-infected women and men (Cozzi

Lepri et al., 1994; Chaisson et al., 1995; Farzadegan et al., 1998; Junghans et al., 1999; Collaborative Group on AIDS Incubation and HIV Survival including the CASCADE EU Concerted Action, 2000). Our findings are consistent with earlier studies, and add spatial detail regarding the 3D distribution and degree of brain atrophy. Oster et al. (1993) demonstrated remarkable atrophy in the central brain nuclei (including striatum and thalamus) and cerebral white matter on examination of autopsied HIV-infected brains. Aylward et al. (1993) demonstrated volumetrically that basal ganglia volumes were smaller in demented AIDS patients than non-demented or control subjects. Immunohistochemically, Kure et al. (1990) found that HIV antigens were more numerous in the globus pallidus than in other sites. In positron emission tomography scans of HIV-infected patients, there was significant asymmetry in glucose utilization in prefrontal and premotor regions (Pascal et al., 1991). Glucose hypometabolism was also found in the basal ganglia in motor-impaired patients (von Giesen et al., 2000). In a diffusion tensor imaging study, decreased diffusion anisotropy, which suggests microscopic damage in the nerve fiber tracts, was detected in the genu and splenium of the corpus callosum in patients with high viral load (Filippi et al., 2001). Given its proximity to the ventricular CSF, the caudate nucleus is especially vulnerable to attack by HIV, especially in severely immunosuppressed patients (Stout et al., 1998), and a high level of HIV RNA has been found in the caudate (McClernon et al., 2001). Contrary to expectations, we did not detect significant caudate atrophy using TBM, although we have detected it using surface-based anatomical modeling methods (Becker et al., submitted for publication-a). This may be ascribed to the generally low intensity contrast of the caudate nucleus relative to the adjacent white matter, making it difficult to achieve accurate shape matching using the intensity-based JRD algorithm. We addressed this problem in another study using anatomical mesh modeling methods to match the manually segmented outline surfaces of the caudate nucleus. This made it easier to detect subcortical differences between AIDS and control subjects using radial maps of atrophy (Thompson et al., 1996; Becker et al., submitted for publication-a).

The pathognomonic characteristic of brain HIV infection is the formation of multinucleated giant cells, particularly in hemispheric white matter and basal ganglia (Budka et al., 1987; Lawrence and Major, 2002; Bell, 2004). These changes are accompanied by infiltration of lymphocytes, astrocytes and microglia/macrophages. The activated microglia and macrophages induce myelin and axonal damage, and ultimately neuronal apoptosis, which accounts for the majority of brain atrophy in HIV-associated dementia (Ozdener, 2005). Our findings of white matter atrophy in primary sensory and motor, medial frontal and premotor regions may be secondary to the significant thinning in corresponding cortices (Thompson et al., 2005). Taken together with the tissue loss in the corpus callosum, where commissural fibers interconnect opposite cortices, cortical neuronal loss may lead to Wallerian degeneration (Bramlett and Dietrich, 2002). This may contribute to white matter atrophy, exacerbating the direct effects of viral replication and inflammatory damage in the white matter.

Although white matter abnormalities are commonly seen on MRI in AIDS patients, only a few studies have associated white matter change with cognitive impairment. Aylward et al. (1995) showed that the white matter volume in demented AIDS patients was less than in those who were non-demented. Harrison et al. (1998) found that patients who performed poorly on neurocognitive tests were more likely to have T2-hyperintense white matter abnormalities on MRI. Neither of these studies specified white matter regions associated with this neuropsychological impairment. Neuroimaging techniques sensitive to molecular content, such as magnetic resonance spectroscopy, have been more revealing. Chang et al. (1999) detected elevated myoinositol and choline levels in frontal white matter, suggesting glial proliferation and cell membrane injury, when patients had only mild cognitive dysfunction. These metabolites in frontal white matter correlated with $CD4^+$ count and CSF,

but not plasma viral load. Apparently, the more standard structural MRI techniques lack the requisite sensitivity to detect the full range of white matter abnormalities associated with HIV cognitive impairment (Paul et al., 2002). When TBM is used in conjunction with conventional MRI, it can be sufficiently sensitive to map the profile of atrophy and can help visualize the spatial correlation patterns in patients with mild to moderate cognitive dysfunction.

HIV-associated dementia tends to develop when $CD4^+$ T-lymphocyte number falls below 200 cells/μl (Childs et al., 1999; Dore et al., 1999), and in this study, $CD4^+$ count correlated with the severity of cognitive impairment. This relationship may be partially ascribed to poor general condition or concurrent systemic opportunistic infections influencing neuropsychological performance in AIDS patients. Even so, cognitive impairment may also result from white matter atrophy (and associated cortical atrophy) which occurs in parallel with HIV-induced depletion of $CD4^+$ cells (the rate of these two processes may not be connected, but both are caused by HIV). The $CD4^+$ T-cell number reflects patients' neurological status (Lopez et al., 1999; Becker et al., submitted for publication-b). White matter loss was greater in patients with $CD4^+$ counts less than 200 cells/μl-relative to those with better immune function and $CD4^+$ counts around 500 cells/μl (Stout et al., 1998). Depressed $CD4^+$ counts coincided with reduced cerebral blood flow on perfusion MRI in temporoparietal regions (Chang et al., 2000). Low $CD4^+$ T-cell number indicates active HIV replication, which enhances the chance of hematogenous seeding and damage to the brain over time. However, in our study, gray or white matter atrophy was not related to the plasma viral load, which may be due to waxing and waning pattern of plasma viral RNA level in patients undergoing treatment. Moreover, viral RNA level in plasma or peripheral tissues may not reflect the degree of brain damage, or AIDS dementia, as effectively as levels measured in brain tissues or CSF (Brew et al., 1997; Chang et al., 1999; McClernon et al., 2001).

Half of our patients were receiving HAART. HAART restores immune function, reducing opportunistic infections, and has prolonged the median survival period for patients to 44 months in contrast to 6 months in the pre-HAART era (Dore et al., 2003). The prevalence and incidence of HIV-associated dementia have also decreased since HAART was introduced (Maschke et al., 2000; Sacktor et al., 2001). In a cohort study, patients taking HAART for 3 years showed significant improvement in neurocognitive performance, which was associated with the magnitude of $CD4^+$ cell count increases (Cohen et al., 2001). However, whether HAART can prevent neuropathological progression is controversial. HIV encephalitis/encephalopathy is still prevalent in 25% autopsied brains in the HAART era (Masliah et al., 2000). Furthermore, there is a rising prevalence of a "burn-out" form of HIV encephalopathy in which the neuronal degeneration persists and even worsens despite undetectable viral load (Neuenburg et al., 2002; Gray et al., 2003; Brew, 2004). We found no difference in brain atrophy between patients receiving HAART or not. Though our sample was small and currently cross-sectional, our results imply that HAART may not save brain tissue, at least not to a substantial degree, but it is still positive in improving neurocognitive function indirectly and bolsters $CD4^+$ T-cell immunity.

AIDS patients may have an increased risk of accelerated brain aging and developing Alzheimer's disease (Brew, 2004). Possible reasons include elevated level of cholesterol and triglyceride as a side effect of protease inhibitor use, axonal injury in HIV encephalitis, and depression in activity of beta-amyloid degrading enzymes by HIV regulatory proteins (Rempel and Pulliam, 2005). Activated macrophages and microglia and elevated cytokine levels induced by HIV infection may also aggravate neuronal apoptosis (Ozdener, 2005). In our healthy subjects, regional brain volumes were negatively correlated with age in frontal and temporal lobes and in the posterior limbs of the internal capsule, as has commonly been

reported in volumetric (Scahill et al., 2003), voxel-based morphometric (Good et al., 2001) and cortical thickness (Sowell et al., 2003) studies. We were surprised that we did not find such an age effect in the AIDS group, although there were more patients than controls. This may be due to high intersubject variance, small sample size, and the restricted age range assessed. These may have masked any true statistical relationship.

In this study, we demonstrated disease-related atrophy in various white matter regions in HIV/AIDS using TBM before any T1 or T2 lesions were present on MRI. Nevertheless, the deformation algorithm infers atrophy based on changes in tissue boundaries, rather than true changes in white matter signal or physiological integrity. DTI (Filippi et al., 2001), MR spectroscopy (Chang et al., 1999), or relaxometric studies (Wilkinson et al., 1996) may be beneficial to assess tissue integrity in the white matter in AIDS, and to understand the origin of any intrinsic molecular changes occurring at a local level in the white matter.

Technical considerations

Advantages of JRD as a registration measure—Fig. 4 compares how well disease effects are detected when different registration approaches are used to drive the image deformation. The plots in the figure are based on the idea underlying the false discovery rate approach (Nichols and Hayasaka, 2003), in the sense that the set of significance values in a statistical map are sorted into numerical order and their cumulative histogram is compiled. Subject to some reasonable assumptions, it is legitimate to compare the cumulative histograms of the maps generated using different registration procedures. Here we compared significance maps created by using different alpha parameters in the registration cost function, as these correspond to the JRD cost function when alpha is not equal to 1, and mutual information when alpha is 1. The cumulative significance plot for maps made with the JRD cost function rises more steeply at very low probability values, meaning that relative to more standard registration cost functions – such as mutual information (MI) and the sum of squared differences in image intensities (SSD) – it is giving a higher number of voxels with very highly significant effects at the voxel level. As such it is worth considering the use of JRD, in addition to more standard registration cost functions, for tensor-based morphometry. The MI cost function outperforms SSD, which is also natural given that the MRI joint signal distribution is not likely to be a straight line when the images are registered, as SSD assumes. A final observation is that the number of voxels significant at P=0.01 in the significance histograms is greatly diminished as alpha is reduced drastically below 0.95, and this relationship appears to be monotonically decreasing with decreasing alpha below 0.95, suggesting worse registration and impaired detection of group differences (which relies on good registration). The comparison of cumulative significance plots is valuable for ranking methods but relies on the assumption that the significance maps generated by the different registration techniques cannot be regarded as perfectly registered with each other, so there could be some (minor) bias in the extent and position of the detected effects, which could affect the cumulative significance plot. We also note that the experiments using cumulative distribution functions (CDFs) of P values suggest that more voxels show significance at the conventional voxel level when JRD is used as the registration cost function, but it would require multiple independent statistical contrasts to confirm this, as well as assurances that the increased power was not attributable to poorer registration (this issue is addressed by the experiments that assess voxel overlap as a measure of registration accuracy). In other words, it would be valuable to show, in multiple independent contrasts, that JRD repeatedly gave rise to more suprathreshold voxels than MI or other cost functions for TBM. More empirical data are required to compute the many contrasts required to show significant differences in power, and we will attempt to test this as the large quantity of data required accumulates in future studies.

Implementation—In our algorithm we take $w(i_1)=p(i_1)$ as the weight function used in the definition of the JRD. Although He et al. (2003) showed that, when the two images are exactly matched, the JRD is largest if a uniform weight is taken, we found that $w(i_1)=1$ failed to achieve a satisfactory matching of the images, which may indicate that the magnitude of the JRD is not the only factor that influences the registration process before the endpoint is achieved. Nevertheless, other choices of weight functions are possible.

Global scaling—To facilitate convergence (i.e., avoid local minima of the cost function), before nonlinear deformation, the images were first aligned using affine registration with scaling in *x*-, *y*-, and *z*- directions. This is a standard step in nonlinear image registration, where the linear term is fitted prior to estimating the nonlinear parameters. This accelerates convergence and avoids local minima. So, although the warps can be estimated on the native space data, a 9-parameter fit was used to avoid misregistrations due to the deformation field settling in non-global local minima of the cost function. As there was no global difference in total brain volume (global scale) between AIDS and control subjects, we discounted the global term to reduce non disease-related variance, as is somewhat standard in voxel-based morphometric studies.

Statistics—In our experiments we used a univariate statistic to evaluate the group differences in the local Jacobian determinant of the deformation fields. However, a multivariate Hotelling's T^2 test is an alternative way of analyzing deformations. Hotelling's T^2 statistics have been applied to build parametric null distributions for the displacement vectors in deformation morphometry (Thompson et al., 1997; Cao and Worsley, 1999; Kumar et al., 2003) and parametric null distributions for the displacement velocity fields (Chung et al., 2001), based on Gaussian random field theory. There has also been work deriving analytic formulae giving *P* values for maxima based on suprathreshold statistics in fields of Hotelling's T^2 statistics, and these formulae have been applied successfully in deformation morphometry (Cao, PhD Thesis, McGill University, 1997). Since the whole Jacobian tensor typically contains more information than its determinant, multivariate statistical approaches on the tensor fields may yield larger effect sizes and help detect subtle brain changes in disease (Gaser et al., 2001). Other work has focused on characterizing global spatial effects in image deformations, via principal components analysis or canonical variates analysis (Ashburner et al., 1998).

In conclusion, though our results are based on a small number of subjects, we demonstrated that TBM, based on using the JRD registration method, facilitates visualization of brain structural alterations associated with HIV. In future we expect to evaluate more subjects, especially women, to identify any sex differences in the effects, if present. TBM may hold promise for monitoring CNS disease progression in AIDS and perhaps also for gauging the effect of neuroprotective agents (e.g., NMDA-receptor antagonists) in future clinical trials. The JRD method is robust for fluid image registration in terms of boundary correspondence, resistance to noise, and utility for clinical studies. Our algorithm applies to various 2D and 3D geometric shapes and real MRI images as shown here by mapping abnormal brain morphology in HIV/AIDS patients relative to normal controls. In the future, we will evaluate our generalized information-theoretic method with registrations of multi-modality clinical images, such as MRI and PET data.

Acknowledgments

This research was supported by the National Institute on Aging (AG021431 to J.T.B. and AG016570 to P.M.T.), the National Library of Medicine, the National Institute for Biomedical Imaging and Bioengineering, and the National Center for Research Resources (LM05639, EB01651, RR019771 to P.M.T.). M.C.C. was also generously supported by a fellowship from the Government of Taiwan. J.T.B. was the recipient of a Research Scientist Development Award-Level II (MH01077).

Appendix

Derivation of Eq. (3)

If we set $w(i_1)=p(i_1)$, with $p_u(i_2|i_1)=\frac{p_u(i_1,i_2)}{p(i_1)}$ and $p_u(i_2)=\int_R p_u(i_1,i_2)di_1$, Eq. (2) becomes

$$
\begin{aligned}
D_\alpha(u)=&\frac{1}{1-\alpha}\log\lfloor\int_R\left(\int_R w(i_1)p_u(i_2|i_1)di_1\right)^\alpha di_2\rfloor\\
&-\int_R w(i_1)\left(\frac{1}{1-\alpha}\log\left(\int_R p_u(i_2|i_1)^\alpha di_2\right)\right)di_1\\
=&\frac{1}{1-\alpha}\log\lfloor\int_R\left(\int_R p(i_1)p_u(i_2|i_1)di_1\right)^\alpha di_2\rfloor\\
&-\int_R p(i_1)\left(\frac{1}{1-\alpha}\log\left(\frac{1}{p(i_1)^\alpha}\int_R p_u(i_1,i_2)^\alpha di_2\right)\right)di_1\\
=&\frac{1}{1-\alpha}\log\left[\int_R p_u(i_2)^\alpha di_2\right]\\
&-\frac{1}{1-\alpha}\int_R p(i_1)\left[\log\left(\int_R p_u(i_1,i_2)^\alpha di_2\right)-\log(p(i_1)^\alpha)\right]di_1\\
=&\frac{1}{1-\alpha}\left\{\log\left(\int_R p_u(i_2)^\alpha di_2\right)-\int_R p(i_1)\log\left(\int_R p_u(i_1,i_2)^\alpha di_2\right)di_1+\alpha\int_R p(i_1)\log p(i_1)di_1\right\}.
\end{aligned}
\tag{15}
$$

Derivation of Eq. (6)

If **w** a small perturbation of **u**, taking the definition of the first variation of $\tilde{D}_\alpha(\mathbf{u})$ and Eq. (3) together, with $\frac{\partial p_{\mathbf{u}+\varepsilon\mathbf{w}}(i_2)}{\partial\varepsilon}=\int_R\frac{\partial p_{\mathbf{u}+\varepsilon\mathbf{w}}(i_1,i_2)}{\partial\varepsilon}di_1$ *and* $\frac{\partial}{\partial\varepsilon}\left(\int_R p(i_1)\log p(i_1)di_1\right)=0$, we have

$$
\begin{aligned}
&\frac{\partial\tilde{D}_\alpha(\mathbf{u}+\varepsilon\mathbf{w})}{\partial\varepsilon}\Big|_{\varepsilon=0}\\
&=-\frac{1}{1-\alpha}\frac{\partial}{\partial\varepsilon}\left\{\log\left(\int_R p_{\mathbf{u}+\varepsilon\mathbf{w}}(i_2)^\alpha di_2\right)-\int_R p(i_1)\log\left(\int_R p_{\mathbf{u}+\varepsilon\mathbf{w}}(i_1,i_2)^\alpha di_2\right)di_1+\alpha\int_R p(i_1)\log p(i_1)di_1\right\}_{\varepsilon=0}\\
&=-\frac{1}{1-\alpha}\left\{\frac{\alpha}{k_{\mathbf{u}+\varepsilon\mathbf{w},\alpha}}\int_R p_{\mathbf{u}+\varepsilon\mathbf{w}}(i_2)^{\alpha-1}\frac{\partial p_{\mathbf{u}+\varepsilon\mathbf{w}}(i_2)}{\partial\varepsilon}di_2-\int_R\frac{p(i_1)}{q_{\mathbf{u}+\varepsilon\mathbf{w},\alpha}(i_1)}\cdot\alpha\left(\int_R p_{\mathbf{u}+\varepsilon\mathbf{w}}(i_1,i_2)^{\alpha-1}\frac{\partial p_{\mathbf{u}+\varepsilon\mathbf{w}(i_1,i_2)}}{\partial\varepsilon}di_2\right)di_1\right\}_{\varepsilon=0}\\
&=-\frac{\alpha}{1-\alpha}\int_{R^2}\left[\frac{p_{\mathbf{u}+\varepsilon\mathbf{w}}(i_2)^{\alpha-1}}{k_{\mathbf{u}+\varepsilon\mathbf{w},\alpha}}-\frac{p(i_1)p_{\mathbf{u}+\varepsilon\mathbf{w}}(i_1,i_2)^{\alpha-1}}{q_{\mathbf{u}+\varepsilon\mathbf{w},\alpha}(i_1)}\right]\frac{\partial p_{\mathbf{u}+\varepsilon\mathbf{w}}(i_1,i_2)}{\partial\varepsilon}\Big|_{\varepsilon=0}di_1di_2,
\end{aligned}
$$

where $k_{\mathbf{u}+\varepsilon\mathbf{w},\alpha}=\int_R p_{\mathbf{u}+\varepsilon\mathbf{w}}(i_2)^\alpha di_2$, and $q_{\mathbf{u}+\varepsilon\mathbf{w},\alpha}(i_1)=\int_R p_{\mathbf{u}+\varepsilon\mathbf{w}}(i_1,i_2)^\alpha di_2$.

References

Arsigny, V.; Fillard, P.; Pennec, X.; Ayache, N. Fast and simple calculus on tensors in the Log-Euclidean framework. Proceedings of the 8th Int. Conf. on Medical Image Computing and Computer-Assisted Intervention—MICCAI 2005; October 26–29; Palm Springs, CA, USA. 2005.

Ashburner J, Friston KJ. Nonlinear spatial normalization using basis functions. Hum. Brain Mapp. 1999; 7(4):254–266. [PubMed: 10408769]

Ashburner J, Friston KJ. Voxel-based morphometry—The methods. NeuroImage. 2000; 11(6):805–821. [PubMed: 10860804]

Ashburner J, Hutton C, Frackowiak R, Johnsrude I, Price C, Friston K. Identifying global anatomical differences: deformation-based morphometry. Hum. Brain Mapp. 1998; 6(5–6):348–357. [PubMed: 9788071]

Avants B, Gee JC. Geodesic estimation for large deformation anatomical shape averaging and interpolation. NeuroImage. 2004; 23 Suppl. 1:S139–S150. [PubMed: 15501083]

Avants BB, Schoenemann PT, Gee JC. Lagrangian frame diffeomorphic image registration: Morphometric comparison of human and chimpanzee cortex. Med. Image Anal. 2006; 10(3):397–412. [PubMed: 15948659]

Aylward EH, Henderer JD, McArthur JC, Brettschneider PD, Harris GJ, Barta PE, Pearlson GD. Reduced basal ganglia volume in HIV-1-associated dementia: results from quantitative neuroimaging. Neurology. 1993; 43(10):2099–2104. [PubMed: 8413973]

Aylward EH, Brettschneider PD, McArthur JC, Harris GJ, Schlaepfer TE, Henderer JD, Barta PE, Tien AY, Pearlson GD. Magnetic resonance imaging measurement of gray matter volume reductions in HIV dementia. Am. J. Psychiatry. 1995; 152(7):987–994. [PubMed: 7793469]

Becker JT, Sanchez J, Dew MA, Lopez OL, Dorst SK, Banks G. Neuropsychological abnormalities among HIV-infected individuals in a community-based sample. Neuropsychology. 1997; 11(4): 592–601. [PubMed: 9345703]

Becker JT, Hayashi KM, Seaman JL, Lopez OL, Aizenstein HJ, Toga AW, Thompson PM. Alterations in hippocampal and caudate nucleus structure in HIV/AIDS revealed by three dimensional mapping. Arch. Neurol. submitted for publication-a.

Becker JT, Juengst S, Aizenstein HJ, Lopez OL. Neuropsychological and Brain Structural Abnormalities in HIV/AIDS. submitted for publication-b.

Bell JE. An update on the neuropathology of HIV in the HAART era. Histopathology. 2004; 45:549–559. [PubMed: 15569045]

Benjamini Y, Hochberg Y. Controlling the false discovery rate: a practical and powerful approach to multiple testing. J. R. Statist. Soc. B. 1995; 57(1):289–300.

Bramlett HM, Dietrich WD. Quantitative structural changes in white and gray matter 1 year following traumatic brain injury in rats. Acta Neuropathol. (Berl.). 2002; 103(6):607–614. [PubMed: 12012093]

Brew BJ. Evidence for a change in AIDS dementia complex in the era of highly active antiretroviral therapy and the possibility of new forms of AIDS dementia complex. AIDS. 2004; 18 Suppl. 1:S75–S78. [PubMed: 15075501]

Brew BJ, Pemberton L, Cunningham P, Law MG. Levels of human immunodeficiency virus type 1 RNA in cerebrospinal fluid correlate with AIDS dementia stage. J. Infect. Dis. 1997; 175(4):963–966. [PubMed: 9086160]

Bro-Nielsen M, Gramkow C. Fast fluid registration of medical images. Proceedings of Visualization in Biomedical Computing (VBC). 1996:267–276.

Budka H, Costanzi G, Cristina S, Lechi A, Parravicini C, Trabattoni R, Vago L. Brain pathology induced by infection with the human immunodeficiency virus (HIV). A histological, immunocytochemical, and electron microscopical study of 100 autopsy cases. Acta Neuropathol. (Berl.). 1987; 75(2):185–198. [PubMed: 3434225]

Cao, J. PhD thesis. Montreal, Canada: McGill University; 1997.

Cao J, Worsley KJ. The detection of local shape changes via the geometry of Hotelling's T^2 fields. Ann. Stat. 1999; 27(3):925–942.

Center for Disease Control and Prevention. Morbid. Mortal. Wkly., Rep. Recomm. Rep. 1992; 41(RR-17):1–19.

Chaisson RE, Keruly JC, Moore RD. Race, sex, drug use, and progression of human immunodeficiency virus disease. N. Engl. J. Med. 1995; 333(12):751–756. [PubMed: 7643881]

Chang L, Ernst T, Leonido-Yee M, Walot I, Singer E. Cerebral metabolite abnormalities correlate with clinical severity of HIV-1 cognitive motor complex. Neurology. 1999; 52(1):100–108. [PubMed: 9921855]

Chang L, Ernst T, Leonido-Yee M, Speck O. Perfusion MRI detects rCBF abnormalities in early stages of HIV-cognitive motor complex. Neurology. 2000; 54(2):389–396. [PubMed: 10668700]

Childs EA, Lyles RH, Selnes OA, Chen B, Miller EN, Cohen BA, Becker JT, Mellors J, McArthur JC. Plasma viral load and CD4 lymphocytes predict HIV-associated dementia and sensory neuropathy. Neurology. 1999; 52(3):607–613. [PubMed: 10025796]

Christensen GE, Rabbitt RD, Miller MI. Deformable templates using large deformation kinematics. IEEE Trans. Image Process. 1996; 5(10):1435–1447. [PubMed: 18290061]

Chung MK, Worsley KJ, Paus T, Cherif C, Collins DL, Giedd JN, Rapoport JL, Evans AC. A unified statistical approach to deformation-based morphometry. NeuroImage. 2001; 14:595–606. [PubMed: 11506533]

Chung MK, Worsley KJ, Robbins S, Paus T, Taylor J, Giedd JN, Rapoport JL, Evans AC. Deformation-based surface morphometry applied to gray matter deformation. NeuroImage. 2003; 18(2):198–213. [PubMed: 12595176]

Chung MK, Dalton KM, Alexander AL, Davidson RJ. Less white matter concentration in autism: 2D voxel-based morphometry. NeuroImage. 2004; 23(1):242–251. [PubMed: 15325371]

Cohen RA, Boland R, Paul R, Tashima KT, Schoenbaum EE, Celentano DD, Schuman P, Smith DK, Carpenter CC. Neurocognitive performance enhanced by highly active antiretroviral therapy in HIV-infected women. AIDS. 2001; 15(3):341–345. [PubMed: 11273214]

Collaborative Group on AIDS Incubation and HIV Survival including the CASCADE EU Concerted Action. Concerted action on SeroConversion to AIDS and death in Europe, 2000. Time from HIV-1 seroconversion to AIDS and death before widespread use of highly-active antiretroviral therapy: a collaborative re-analysis. Lancet. 2000; 355(9210):1131–1137. [PubMed: 10791375]

Collins DL, Peters TM, Evans AC. Automated 3D nonlinear deformation procedure for determination of gross morphometric variability in human brain. Proceedings of The International Society for Optical Engineering (SPIE). 1994; 2359:180–190.

Collins DL, Holmes CJ, Peters TM, Evans AC. Automatic 3-D model-based neuroanatomical segmentation. Hum. Brain Mapp. 1995; 3:190–208.

Cozzi Lepri A, Pezzotti P, Dorrucci M, Phillips AN, Rezza G. HIV disease progression in 854 women and men infected through injecting drug use and heterosexual sex and followed for up to nine years from seroconversion. Italian Seroconversion Study. BMJ. 1994; 309(6968):1537–1542. [PubMed: 7819892]

D'Agostino E, Maes F, Vandermeulen D, Suetens P. A viscous fluid model for multimodal non-rigid image registration using mutual information. Med. Image Anal. 2003; 7:565–575. [PubMed: 14561559]

Davatzikos C, Vaillant M, Resnick SM, Prince JL, Letovsky S, Bryan RN. A computerized approach for morphological analysis of the corpus callosum. J. Comput. Assist. Tomogr. 1996; 20(1):88–97. [PubMed: 8576488]

Davatzikos C, Genc A, Xu D, Resnick SM. Voxel-based morphometry using the RAVENS maps: methods and validation using simulated longitudinal atrophy. NeuroImage. 2001; 14(6):1361–1369. [PubMed: 11707092]

Dore GJ, Correll PK, Li Y, Kaldor JM, Cooper DA, Brew BJ. Changes to AIDS dementia complex in the era of highly active antiretroviral therapy. AIDS. 1999; 13:1249–1253. [PubMed: 10416530]

Dore GJ, McDonald A, Li Y, Kaldor JM, Brew BJ. National HIV Surveillance Committee. Marked improvement in survival following AIDS dementia complex in the era of highly active antiretroviral therapy. AIDS. 2003; 17(10):1539–1545. [PubMed: 12824792]

Edgington, ES. Randomization Tests. 3rd ed.. New York: Marcel Dekker; 1995.

Farzadegan H, Hoover DR, Astemborski J, Lyles CM, Margolick JB, Markham RB, Quinn TC, Vlahov D. Sex differences in HIV-1 viral load and progression to AIDS. Lancet. 1998; 352(9139): 1510–1514. [PubMed: 9820299]

Filippi CG, Ulug AM, Ryan E, Ferrando SJ, van Gorp W. Diffusion tensor imaging of patients with HIV and normal-appearing white matter on MR images of the brain. Am. J. Neuroradiol. 2001; 22(2):277–283. [PubMed: 11156769]

Fletcher PT, Lu C, Pizer SM, Joshi S. Principal geodesic analysis for the study of nonlinear statistics of shape. IEEE Trans. Med. Imag. 2004; 23(8):995–1005.

Fox NC, Crum WR, Scahill RI, Stevens JM, Janssen JC, Rossor MN. Imaging of onset and progression of Alzheimer's disease with voxel-compression mapping of serial magnetic resonance images. Lancet. 2001; 358(9277):201–205. [PubMed: 11476837]

Freeborough PA, Woods RP, Fox NC. Accurate registration of serial 3D MR brain images and its application to visualizing change in neurodegenerative disorders. J. Comput. Assist. Tomogr. 1996; 20(6):1012–1022. [PubMed: 8933812]

Gaser C, Nenadic I, Buchsbaum BR, Hazlett EA, Buchsbaum MS. Deformation-based morphometry and its relation to conventional volumetry of brain lateral ventricles in MRI. NeuroImage. 2001; 13(6 Pt. 1):1140–1145. [PubMed: 11352619]

Genovese CR, Lazar NA, Nichols T. Thresholding of statistical maps in functional neuroimaging using the false discovery rate. NeuroImage. 2002; 15(4):870–878. [PubMed: 11906227]

Good CD, Johnsrude IS, Ashburner J, Henson RN, Friston KJ, Frackowiak RS. A voxel-based morphometric study of ageing in 465 normal adult human brains. NeuroImage. 2001; 14(1 Pt. 1): 21–36. [PubMed: 11525331]

Gray F, Chretien F, Vallat-Decouvelaere AV, Scaravilli F. The changing pattern of HIV neuropathology in the HAART era. J. Neuropathol. Exp. Neurol. 2003; 62(5):429–440. [PubMed: 12769183]

Hall M, Whaley R, Robertson K, Hamby S, Wilkins J, Hall C. The correlation between neuropsychological and neuroanatomic changes over time in asymptomatic and symptomatic HIV-1-infected individuals. Neurology. 1996; 46(6):1697–1702. [PubMed: 8649573]

Hamza AB, Krim H. Image registration and segmentation by maximizing the Jensen–Rényi divergence. Lect. Notes Comput. Sci. 2003; 2683:147–163.

Harrison MJ, Newman SP, Hall-Craggs MA, Fowler CJ, Miller R, Kendall BE, Paley M, Wilkinson I, Sweeney B, Lunn S, Carter S, Williams I. Evidence of CNS impairment in HIV infection: clinical, neuropsychological, EEG, and MRI/MRS study. J. Neurol., Neurosurg. Psychiatry. 1998; 65(3): 301–307. [PubMed: 9728940]

He Y, Hamza AB, Krim H. A generalized divergence measure for robust image registration. IEEE Trans. Signal Process. 2003; 51(5):1211–1220.

Hermosillo, G. PhD thesis. Sophia Antipolis, France: Université de Nice (INRIA-ROBOTVIS); 2002.

Junghans C, Ledergerber B, Chan P, Weber R, Egger M. Sex differences in HIV-1 viral load and progression to AIDS. Swiss HIV Cohort Study. Lancet. 1999; 353(9152):589. [PubMed: 10029004]

Kim B, Boes JL, Frey KA, Meyer CR. Mutual information for automated unwarping of rat brain autoradiographs. NeuroImage. 1997; 5(1):31–40. [PubMed: 9038282]

Kochunov P, Lancaster J, Thompson P, Toga AW, Brewer P, Hardies J, Fox P. An optimized individual target brain in the Talairach coordinate system. NeuroImage. 2002; 17(2):922–927. [PubMed: 12377166]

Kochunov P, Lancaster J, Hardies J, Thompson PM, Woods RP, Cody JD, Hale DE, Laird A, Fox PT. Mapping structural differences of the corpus callosum in individuals with 18q deletions using targetless regional spatial normalization. Hum. Brain Mapp. 2005; 24(4):325–331. [PubMed: 15704090]

Kumar D, Geng X, Christensen GE, Vannier MW. Characterizing shape differences between phantom image populations via multivariate statistical analysis of inverse consistent transformations. Proceedings of the 2nd International Workshop on Biomedical Image Registration (WBIR). 2003:367–376.

Kure K, Weidenheim KM, Lyman WD, Dickson DW. Morphology and distribution of HIV-1 gp41-positive microglia in subacute AIDS encephalitis. Pattern of involvement resembling a multisystem degeneration. Acta Neuropathol. (Berl.). 1990; 80(4):393–400. [PubMed: 2239151]

Lawrence DM, Major EO. HIV-1 and the brain: connections between HIV-1-associated dementia, neuropathology and neuroimmunology. Microbes Infect. 2002; 4:301–308. [PubMed: 11909740]

Leow, AD.; Huang, SC.; Geng, A.; Becker, JT.; Davis, SW.; Toga, AW.; Thompson, PM. Information Processing in Medical Imaging (IPMI) 2005. Colorado: Glenwood Springs; 2005 July 11–15. Inverse consistent mapping in 3D deformable image registration: its construction and statistical properties.

Leow AD, Klunder AD, Jack CR, Toga AW, Dale AM, Bernstein MA, Briston PJ, Gunter JL, Ward CP, Whitwell JL, Borowski B, Fleisher A, Fox NC, Harvey D, Kornak J, Schuff N, Studholme C, Alexander GE, Weiner MW, Thompson PM. for the ADNI Preparatory Phase Study. Longitudinal stability of MRI for mapping brain change using tensor-based morphometry. NeuroImage. 2006; 31(2):627–640. [PubMed: 16480900]

Lopez OL, Wess J, Sanchez J, Dew MA, Becker JT. Neurological characteristics of HIV-infected men and women seeking primary medical care. Eur. J. Neurol. 1999; 6(2):205–209. [PubMed: 10053233]

Lorenzen, P.; Davis, B.; Joshi, S. Model based symmetric information theoretic large deformation multi-modal image registration; Proceedings of IEEE International Symposium on Biomedical Imaging: From Nano to Macro (ISBI); 2004. p. 720-723.

Maschke M, Kastrup O, Esser S, Ross B, Hengge U, Hufnagel A. Incidence and prevalence of neurological disorders associated with HIV since the introduction of highly active antiretroviral therapy (HAART). J. Neurol., Neurosurg. Psychiatry. 2000; 69(3):376–380. [PubMed: 10945813]

Masliah E, DeTeresa RM, Mallory ME, Hansen LA. Changes in pathological findings at autopsy in AIDS cases for the last 15 years. AIDS. 2000; 14(1):69–74. [PubMed: 10714569]

Mazziotta J, Toga A, Evans A, Fox P, Lancaster J, Zilles K, Woods R, Paus T, Simpson G, Pike B, Holmes C, Collins L, Thompson P, MacDonald D, Iacoboni M, Schormann T, Amunts K, Palomero-Gallagher N, Geyer S, Parsons L, Narr K, Kabani N, Le Goualher G, Boomsma D, Cannon T, Kawashima R, Mazoyer B. A probabilistic atlas and reference system for the human brain: International Consortium for Brain Mapping (ICBM). Philos. Trans. R. Soc. London, Ser. B Biol. Sci. 2001; 356(1412):1293–1322. [PubMed: 11545704]

McArthur JC, Brew BJ, Nath A. Neurological complications of HIV infection. Lancet Neurol. 2005; 4(9):543–555. [PubMed: 16109361]

McClernon DR, Lanier R, Gartner S, Feaser P, Pardo CA, St Clair M, Liao Q, McArthur JC. HIV in the brain: RNA levels and patterns of zidovudine resistance. Neurology. 2001; 57(8):1396–1401. [PubMed: 11673579]

Miller MI. Computational anatomy: shape, growth, and atrophy comparison via diffeomorphisms. NeuroImage. 2004; 23 Suppl. 1:S19–S33. [PubMed: 15501089]

Neuenburg JK, Brodt HR, Herndier BG, Bickel M, Bacchetti P, Price RW, Grant RM, Schlote W. HIV-related neuropathology, 1985 to 1999: rising prevalence of HIV encephalopathy in the era of highly active antiretroviral therapy. J. Acquired Immune Defic. Syndr. 2002; 31(2):171–177. [PubMed: 12394795]

Nichols T, Hayasaka S. Controlling the familywise error rate in functional neuroimaging: a comparative review. Stat. Methods Med. Res. 2003; 12(5):419–446. [PubMed: 14599004]

Nichols TE, Holmes AP. Nonparametric permutation tests for functional neuroimaging: a primer with examples. Hum. Brain Mapp. 2001; 15:1–25. [PubMed: 11747097]

Oster S, Christoffersen P, Gundersen HJ, Nielsen JO, Pakkenberg B, Pedersen C. Cerebral atrophy in AIDS: a stereological study. Acta Neuropathol. (Berl.). 1993; 85(6):617–622. [PubMed: 8337940]

Ozdener H. Molecular mechanisms of HIV-1 associated neurodegeneration. J. Biosci. 2005; 30(3): 391–405. [PubMed: 16052077]

Pascal S, Resnick L, Barker WW, Loewenstein D, Yoshii F, Chang JY, Boothe T, Sheldon J, Duara R. Metabolic asymmetries in asymptomatic HIV-1 seropositive subjects: relationship to disease onset and MRI findings. J. Nucl. Med. 1991; 32:1725–1729. [PubMed: 1880574]

Paul R, Cohen R, Navia B, Tashima K. Relationships between cognition and structural neuroimaging findings in adults with human immunodeficiency virus type-1. Neurosci. Biobehav. Rev. 2002; 26(3):353–359. [PubMed: 12034135]

Pluim JPW, Antoine Maintz JB, Viergever MA. *f*-information measures in medical image registration. IEEE Trans. Med. Imag. 2004; 23(12):1508–1516.

Price RW, Brew B, Sidtis J, Rosenblum M, Scheck AC, Cleary P. The brain in AIDS: central nervous system HIV-1 infection and AIDS dementia complex. Science. 1988; 239(4840):586–592. [PubMed: 3277272]

Principe, JC.; Xu, D. Learning from examples with Rényi's information criterion. Proc. of Asilomar Conference on Signals, Systems and Computers; Pacific Grove. 1999. p. 966-970.

Rempel HC, Pulliam L. HIV-1 Tat inhibits neprilysin and elevates amyloid beta. AIDS. 2005; 19(2): 127–135. [PubMed: 15668537]

Sacktor NC, Bacellar H, Hoover DR, Nance-Sproson TE, Selnes OA, Miller EN, Dal Pan GJ, Kleeberger C, Brown A, Saah A, McArthur JC. Psychomotor slowing in HIV infection: a predictor of dementia, AIDS and death. J. NeuroVirol. 1996; 2(6):404–410. [PubMed: 8972422]

Sacktor N, Lyles RH, Skolasky R, Kleeberger C, Selnes OA, Miller EN, Becker JT, Cohen B, McArthur JC. Multicenter AIDS Cohort Study. HIV-associated neurologic disease incidence changes: multicenter AIDS Cohort Study, 1990–1998. Neurology. 2001; 56(2):257–260. [PubMed: 11160967]

Scahill RI, Frost C, Jenkins R, Whitwell JL, Rossor MN, Fox NC. A longitudinal study of brain volume changes in normal aging using serial registered magnetic resonance imaging. Arch. Neurol. 2003; 60(7):989–994. [PubMed: 12873856]

Shattuck DW, Leahy RM. BrainSuite: an automated cortical surface identification tool. Med. Image Anal. 2002; 6(2):129–142. [PubMed: 12045000]

Shen D, Davatzikos C. Very high-resolution morphometry using mass-preserving deformations and HAMMER elastic registration. NeuroImage. 2003; 18(1):28–41. [PubMed: 12507441]

Sowell ER, Peterson BS, Thompson PM, Welcome SE, Henkenius AL, Toga AW. Mapping cortical change across the human life span. Nat. Neurosci. 2003; 6(3):309–315. [PubMed: 12548289]

Storey JD. A direct approach to false discovery rates. J. R. Statist. Soc. B. 2002; 64(Pt. 3):479–498.

Storey, JD.; Tibshirani, R. Technical Report 2001–28. Department of Statistics, Stanford University; 2001. Estimating false discovery rates under dependence, with applications to DNA microarrays.

Stout JC, Ellis RJ, Jernigan TL, Archibald SL, Abramson I, Wolfson T, McCutchan JA, Wallace MR, Atkinson JH, Grant I. the HIV Neurobehavioral Research Center Group. Progressive cerebral volume loss in human immunodeficiency virus infection: a longitudinal volumetric magnetic resonance imaging study. Arch. Neurol. 1998; 55(2):161–168. [PubMed: 9482357]

Studholme C, Cardenas V. A template free approach to volumetric spatial normalization of brain anatomy. Pattern Recogn. Lett. 2004; 25:1191–1202.

Studholme, C.; Cardenas, V.; Schuff, N.; Rosen, H.; Miller, B.; Weiner, M. Detecting spatially consistent structural differences in Alzheimer's and fronto temporal dementia using deformation morphometry; Proceedings of International Conference on Medical Image Computing and Computer Assisted Intervention (MICCAI); 2001. p. 41-48.

Studholme C, Cardenas V, Maudsley A, Weiner M. An intensity consistent filtering approach to the analysis of deformation tensor derived maps of brain shape. NeuroImage. 2003; 19(4):1638–1649. [PubMed: 12948718]

Studholme C, Cardenas V, Blumenfeld R, Schuff N, Rosen HJ, Miller B, Weiner M. Deformation tensor morphometry of semantic dementia with quantitative validation. NeuroImage. 2004; 21(4): 1387–1398. [PubMed: 15050564]

Teipel SJ, Alexander GE, Schapiro MB, Moller HJ, Rapoport SI, Hampel H. Age-related cortical grey matter reductions in non-demented Down's syndrome adults determined by MRI with voxel-based morphometry. Brain. 2004; 127(Pt. 4):811–824. [PubMed: 14985261]

Thompson KA, McArthur JC, Wesselingh SL. Correlation between neurological progression and astrocyte apoptosis in HIV-associated dementia. Ann. Neurol. 2001; 49(6):745–752. [PubMed: 11409426]

Thompson PM, Schwartz C, Toga AW. High-resolution random mesh algorithms for creating a probabilistic 3D surface atlas of the human brain. NeuroImage. 1996; 3:19–34. [PubMed: 9345472]

Thompson PM, MacDonald D, Mega MS, Holmes CJ, Evans AC, Toga AW. Detection and mapping of abnormal brain structure with a probabilistic atlas of cortical surfaces. J. Comput. Assist. Tomogr. 1997; 21(4):567–581. [PubMed: 9216760]

Thompson PM, Giedd JN, Woods RP, MacDonald D, Evans AC, Toga AW. Growth patterns in the developing brain detected by using continuum mechanical tensor maps. Nature. 2000; 404(6774): 190–193. [PubMed: 10724172]

Thompson PM, Dutton RA, Hayashi KM, Toga AW, Lopez OL, Aizenstein HJ, Becker JT. Thinning of the cerebral cortex visualized in HIV/AIDS reflects CD4+ T lymphocyte decline. Proc. Natl. Acad. Sci. U. S. A. 2005; 102(43):15647–15652. [PubMed: 16227428]

Thompson PM, Dutton RA, Hayashi KM, Lu A, Lee SE, Lee JY, Lopez OL, Aizenstein HJ, Toga AW, Becker JT. 3D mapping of ventricular and corpus callosum abnormalities in HIV/AIDS. NeuroImage. 2006; 31(1):12–23. [PubMed: 16427319]

Twining, CJ.; Cootes, T.; Marsland, S.; Petrovic, V.; Schestowitz, R.; Taylor, CJ. Information Processing in Medical Imaging (IPMI) 2005. Colorado: Glenwood Springs; 2005 July 11–15. A unified information-theoretic approach to groupwise non-rigid registration and model building.

Viola P, Wells WM III. Alignment by maximization of mutual information. Int. J. Comput. Vis. 1997; 24(2):137–154.

von Giesen HJ, Antke C, Hefter H, Wenserski F, Seitz RJ, Arendt G. Potential time course of human immunodeficiency virus type 1-associated minor motor deficits: electrophysiologic and positron emission tomography findings. Arch. Neurol. 2000; 57(11):1601–1607. [PubMed: 11074792]

White DA, Heaton RK, Monsch AU. Neuropsychological studies of asymptomatic human immunodeficiency virus-type-1 infected individuals. J. Int. Neuropsychol. Soc. 1995; 1(3):304–315. [PubMed: 9375225]

Wilkinson ID, Paley MN, Hall-Craggs MA, Chinn RJ, Chong WK, Sweeney BJ, Kendall BE, Miller RF, Newman SP, Harrison MJ. Cerebral magnetic resonance relaxometry in HIV infection. Magn. Reson. Imaging. 1996; 14(4):365–372. [PubMed: 8782174]

Woods RP. Characterizing volume and surface deformations in an atlas framework: theory, applications, and implementation. NeuroImage. 2003; 18(3):769–788. [PubMed: 12667854]

Woods RP, Cherry SR, Mazziotta JC. Rapid automated algorithm for aligning and reslicing PET images. J. Comput. Assist. Tomogr. 1992; 16(4):620–633. [PubMed: 1629424]

Woods RP, Grafton ST, Holmes CJ, Cherry SR, Mazziotta JC. Automated image registration: I. General methods and intrasubject, intramodality validation. J. Comput. Assist. Tomogr. 1998; 22(1):139–152. [PubMed: 9448779]

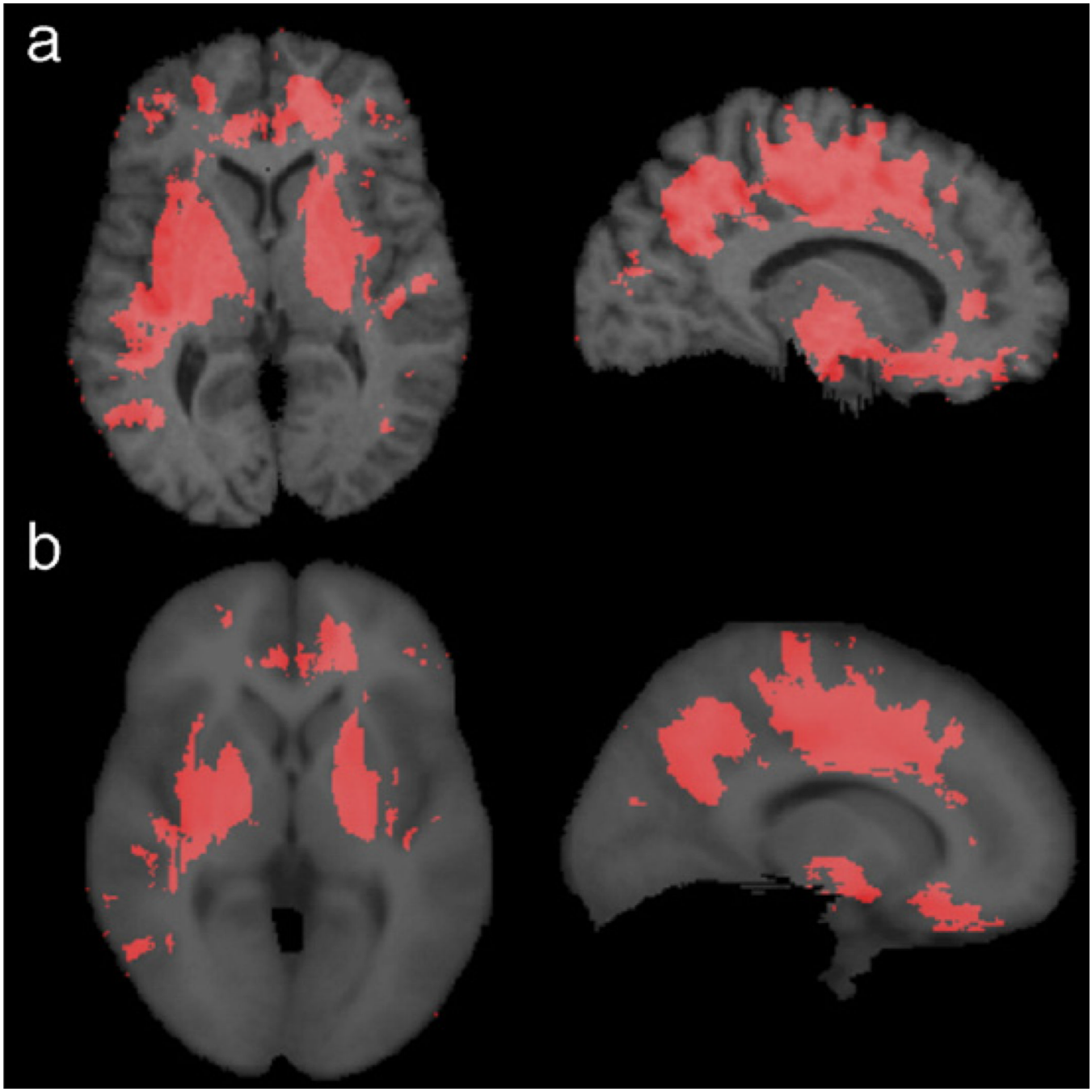

Fig. 1.

This figure shows significance maps computed after using (a) a single subject and (b) the average ICBM53 atlas brain as the registration target image, based on applying the Mann–Whitney *U* test, at each voxel, to the difference in the mean log Jacobian determinant between AIDS and control groups. Only voxels with $P < 0.01$ are displayed (red). Although using an average brain image as the target avoids the bias toward the particular geometry of a single subject, it led to (slightly) lower effect sizes. This is apparent in the subcortical gray matter where the intensity contrast with the surrounding white matter is lower in the average brain. However, the results using each template are very similar in their overall spatial extent and distribution. Template optimization for TBM, e.g., using “minimal deformation

targets" (MDT) (Kochunov et al., 2002), and geodesic mean templates (Avants and Gee, 2004; Fletcher et al., 2004) is the subject of on-going study, by our group and others.

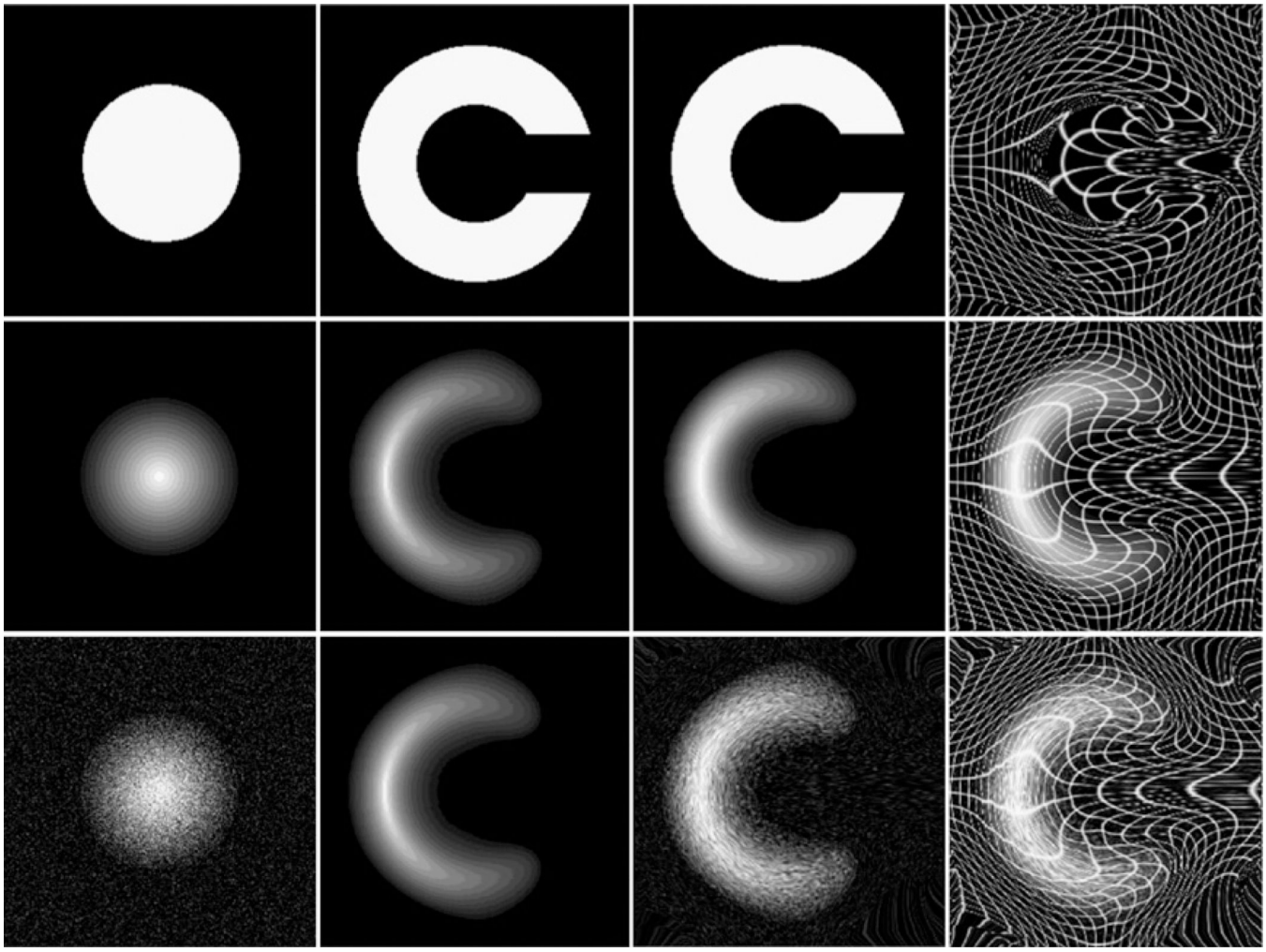

Fig. 2.
Circle to “C” experiments using JRD. From left to right: source image, target image, source deformed to match target, and the deformation applied to a rectangular grid with or without the deformed source. Top row: binary images. Middle: gray-level images with the intensity of the central layer set equal to 255 and reduced by 15 layer by layer. Bottom: test images (the same as in the middle row) show good performance with Gaussian noise added to the source image (SNR=1.92 dB).

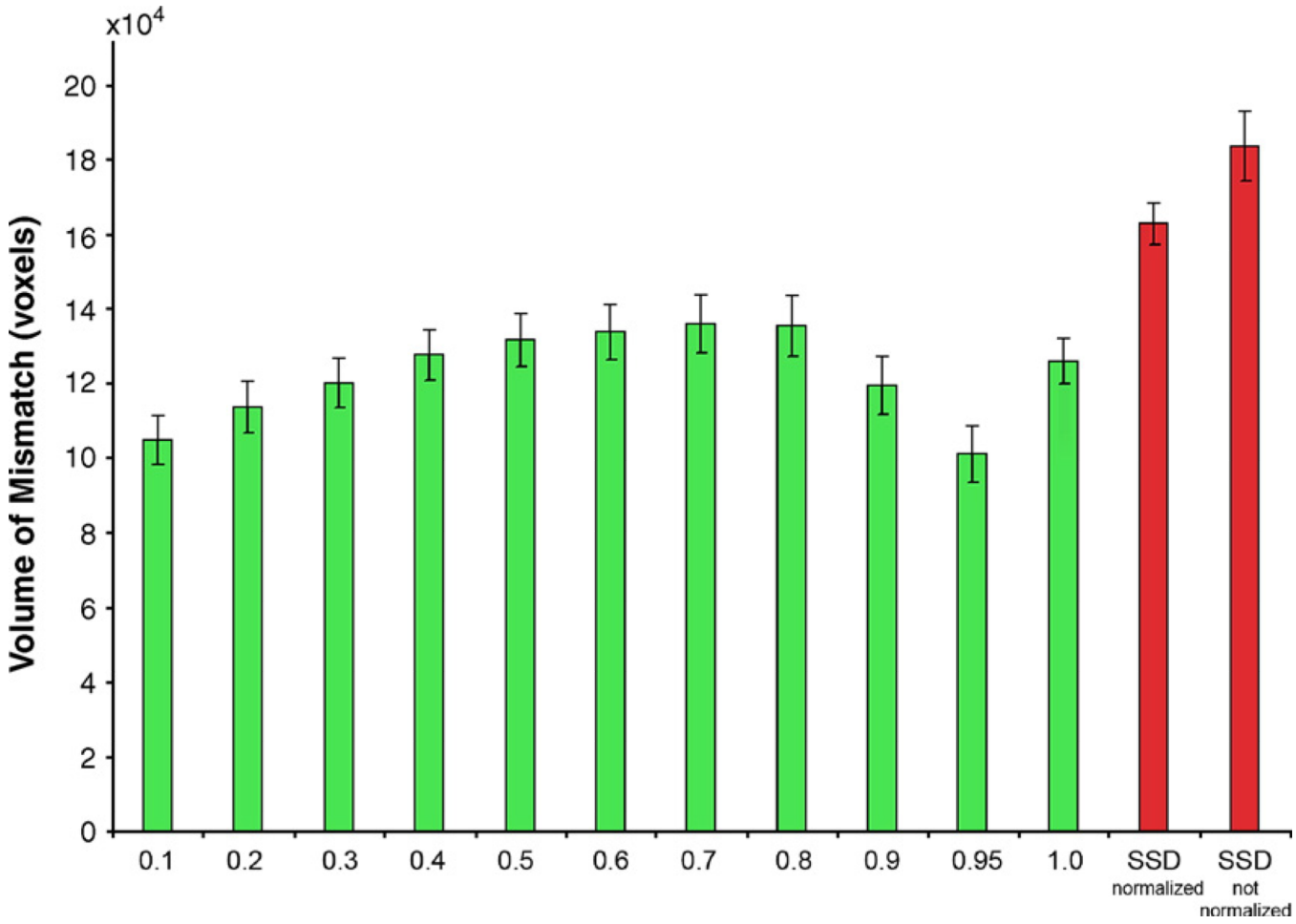

Fig. 3.

The volume of mismatch between the registered source and target brain MR images for different values of α in the cost functional (Jensen–Rényi divergence; green bars) used to align the images. α=1 represents the mutual information. The volume of mismatch based on minimizing the summed squared intensity differences (SSD; red bars) is plotted for reference (SSD is a simpler cost functional, often used in linear and nonlinear image registration, see, e.g., Woods et al., 1998; Ashburner and Friston, 1999 for examples in brain mapping). To allow better registration performance using SSD, prior to image deformation, intensities in the two images were scaled (i.e., intensity normalized) such that the mean intensities over the brain were the same. Although the registration accuracy based on SSD is improved after the image intensities are normalized, the performance of JRD in the 3D experiments is still better than that of SSD, at least on this dataset.

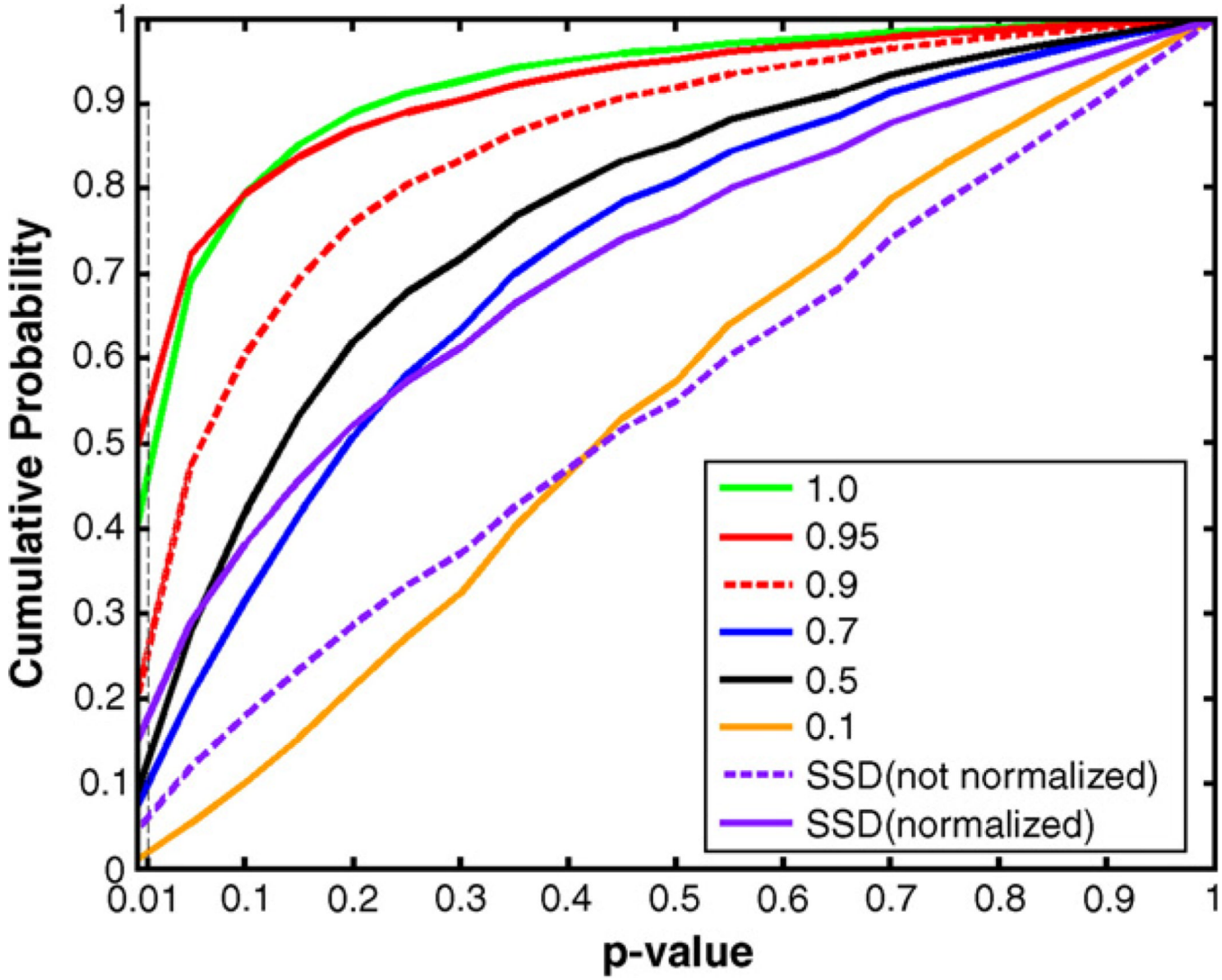

Fig. 4.

Comparisons of JRD at different α values and SSD (with intensity normalized or not normalized), based on the cumulative histogram of the probability maps. The probability maps were obtained from the difference of the mean log Jacobian determinant between the AIDS and control groups, using the Mann–Whitney *U* test. α=1 represents the mutual information. The number of voxels with statistical significance ($P<0.01$) is greatest at α=0.95. Although the computation time using SSD (about 10 min) is shorter than JRD (about 12 min), it is less powerful for detecting disease effects, at least in this study, using the intuitive metric of the number of significant voxels that pass a predetermined primary threshold.

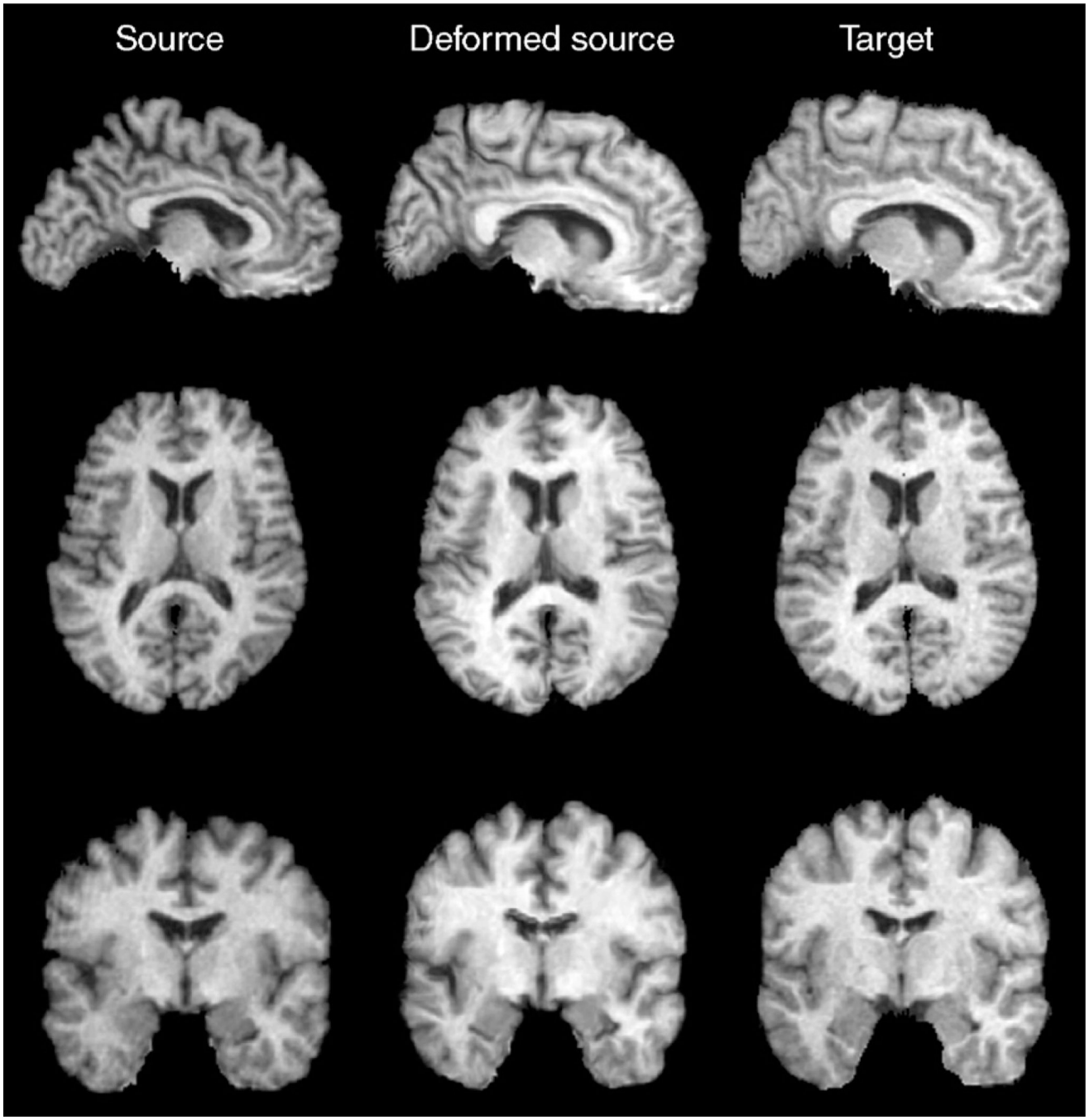

Fig. 5.
Example of 3D registration by the JRD method. On comparison of different sections of the source, deformed source and the target images, registration using the JRD method allows good geometrical matching of the shape of gyri, corpus callosum, and ventricles. Whether cortical homology is established is a more complex issue, but the boundaries are clearly matched with much greater accuracy and boundary correspondence than prior to registration.

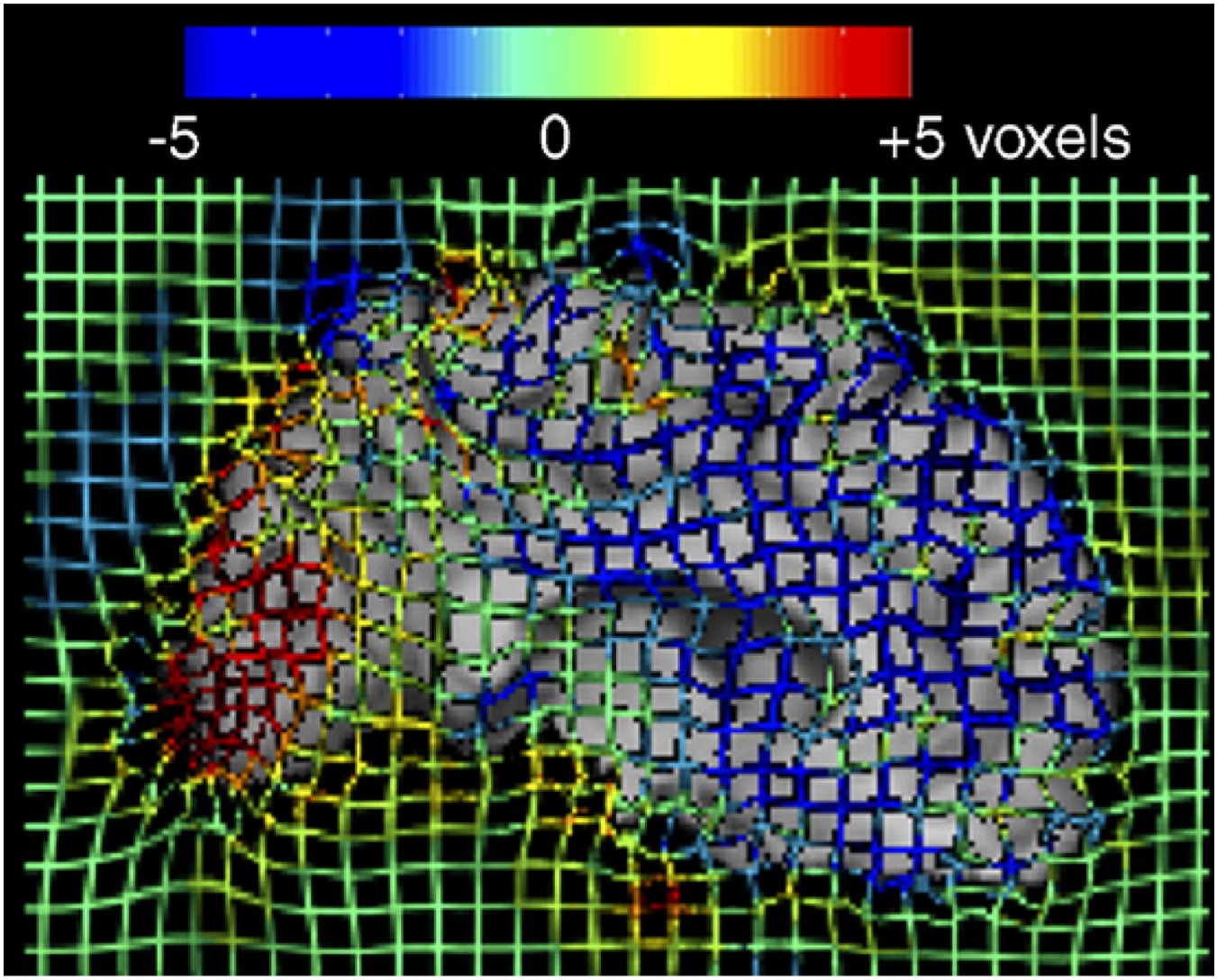

Fig. 6.

To better visualize the 3D deformation field used to drive the registration shown in Fig. 5, a colored grid was superimposed on the registered image. Red and blue colors represent deformation orthogonal to the midsagittal plane of the brain (out of the page).

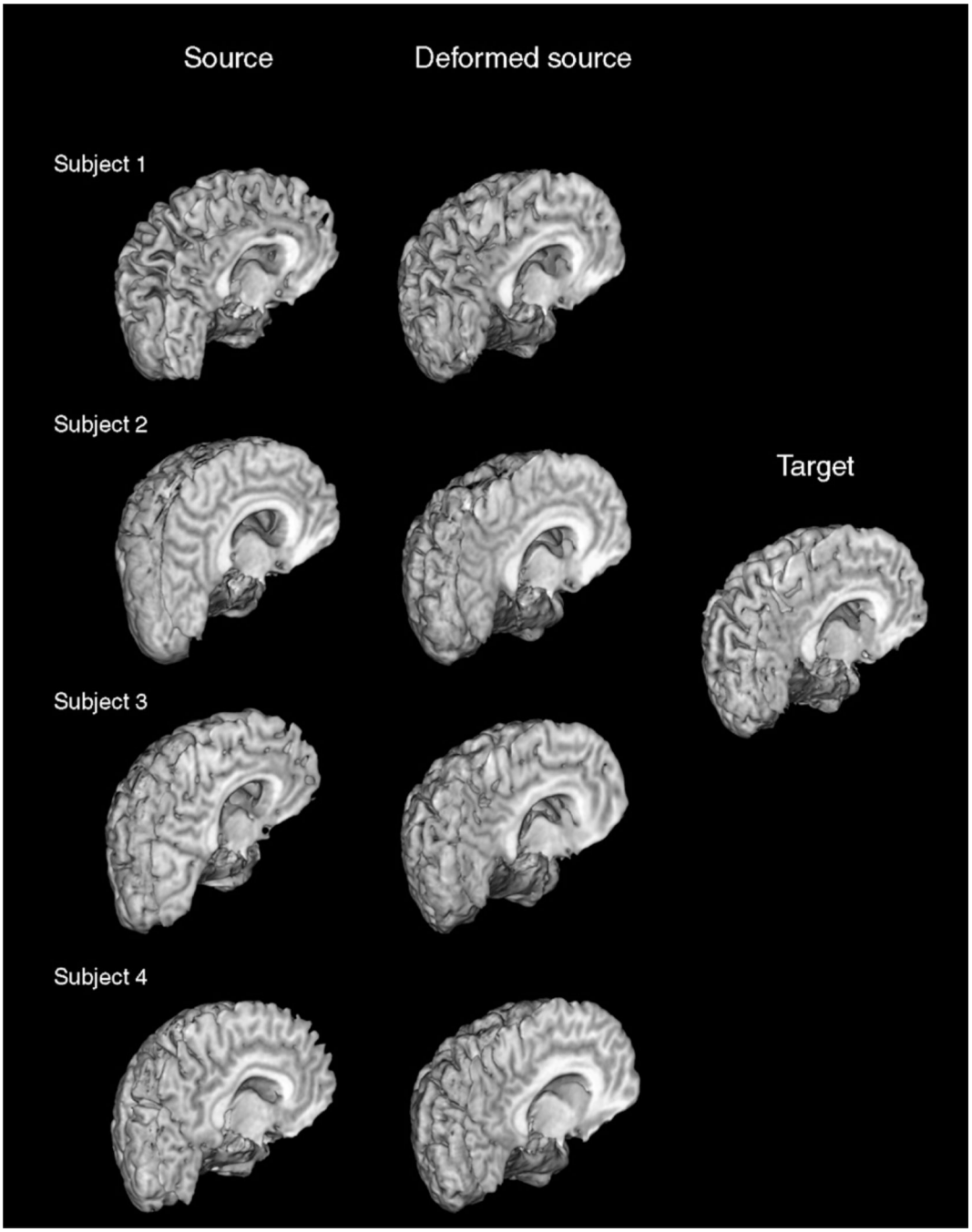

Fig. 7.
3D surfaces of the source, deformed source and the target brain images in several subjects, showing that the gyri, ventricles, and corpus callosum in the source images, are deformed to match the corresponding structures in the target images.

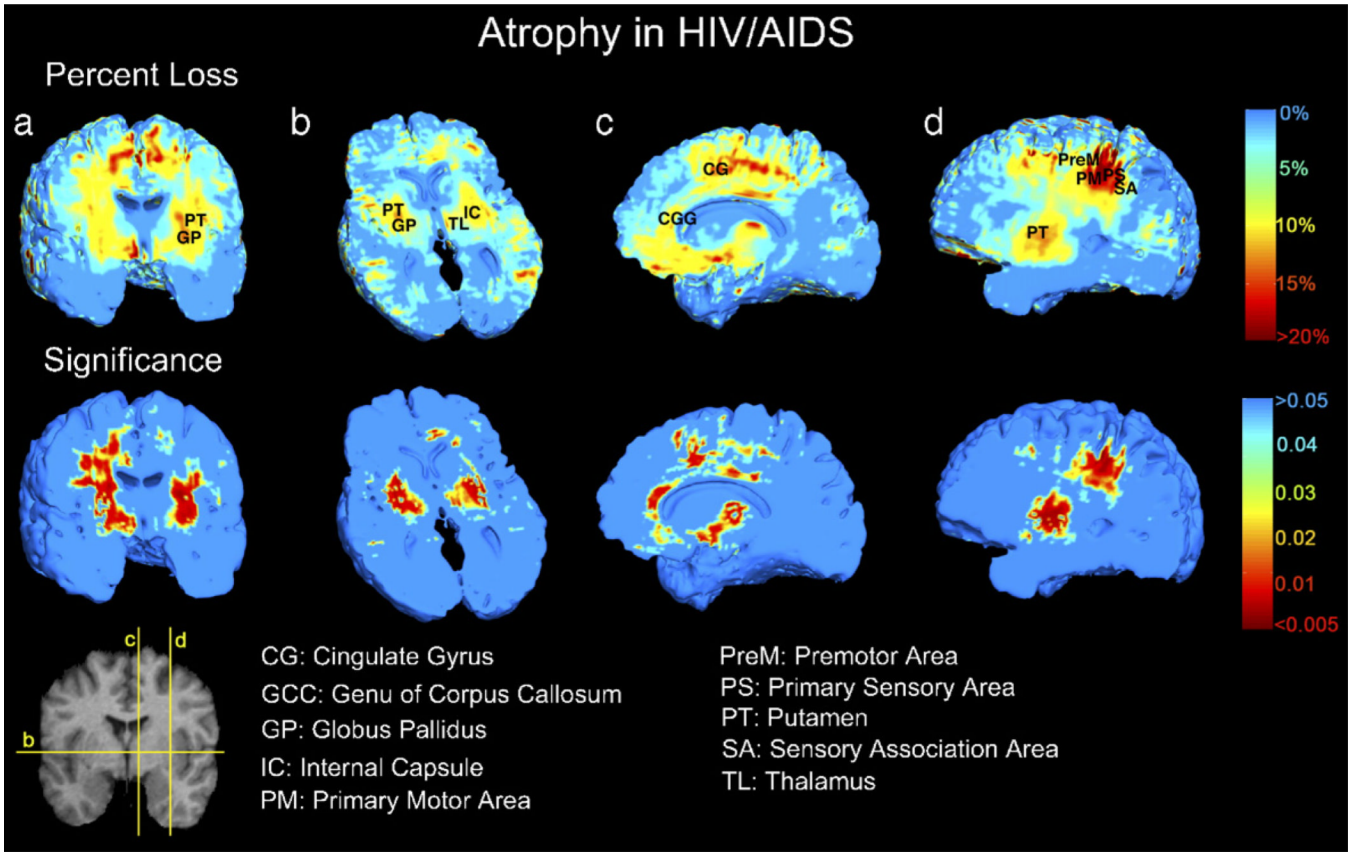

Fig. 8.

Visualization of brain tissue loss in HIV/AIDS. This analysis of disease effects was performed in male subjects only to better control for any possible effects of age and gender. The ratio of the mean Jacobian determinant in AIDS to the mean Jacobian determinant in control subjects was computed voxelwise to map the 3D profile of brain tissue reduction (upper row). Bilateral local atrophy was identified in (a) the putamen, globus pallidus, (b) thalamus, and in the posterior limb of the internal capsule, along with (c) the cingulate gyrus and the genu and mid-posterior body of corpus callosum, and in (c and d) basal and medial frontal lobes. Greatest tissue loss occurs in primary motor and sensory, premotor and sensory association areas (d). Mann–Whitney *U* test was used to obtain the significance map (lower row).

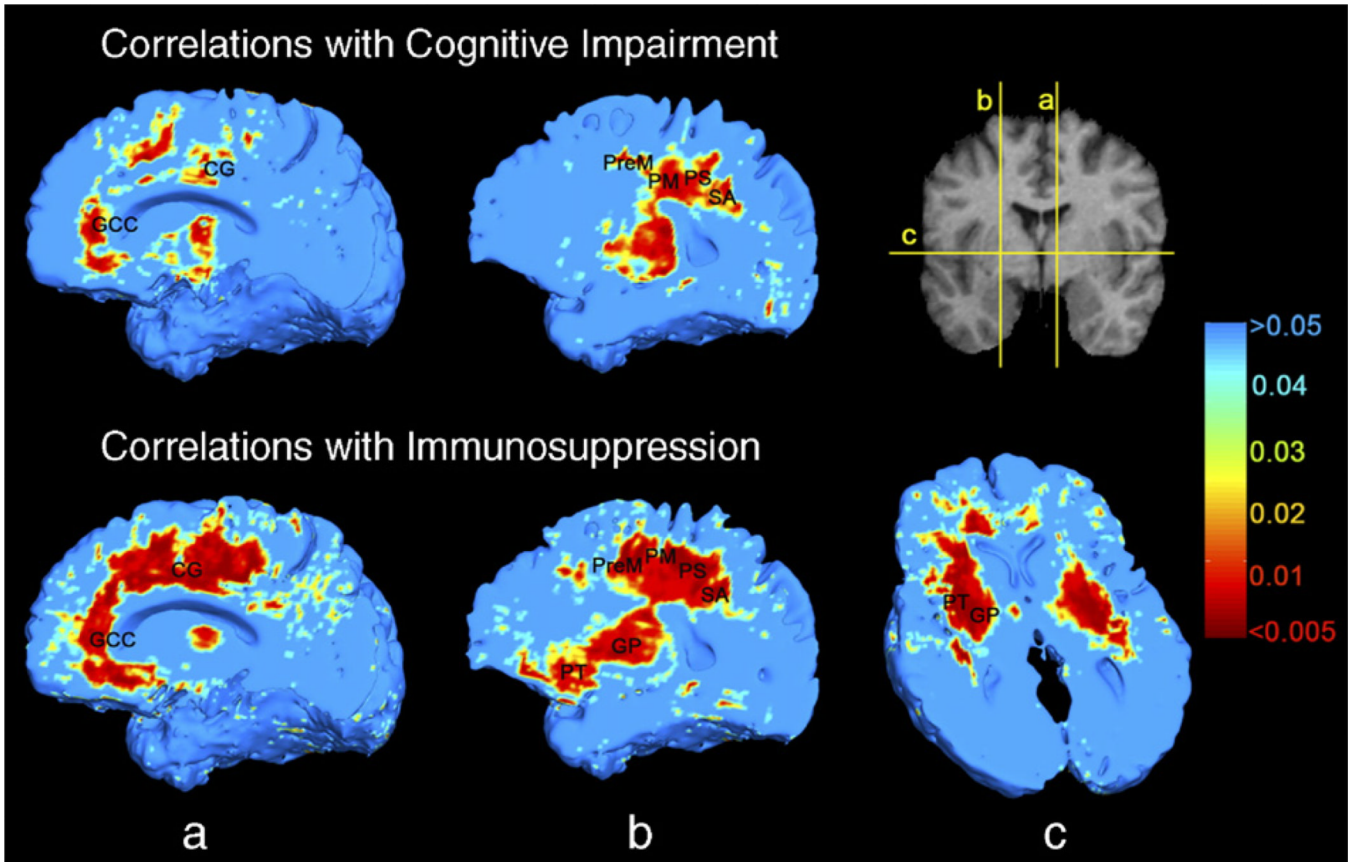

Fig. 9.

Greater brain atrophy is associated with greater cognitive impairment (upper row), in middle cingulate, genu of the corpus callosum, medial and basal frontal lobes, and primary and association sensorimotor areas, tested by Spearman's (non-parametric) rank correlation. Correlations of brain atrophy with $CD4^+$ T-lymphocyte depletion are more extensive in the above regions, as well as in the putamen and globus pallidus (lower row). This analysis was performed within the HIV/AIDS patient group only. Abbreviations are the same as in Fig. 8.

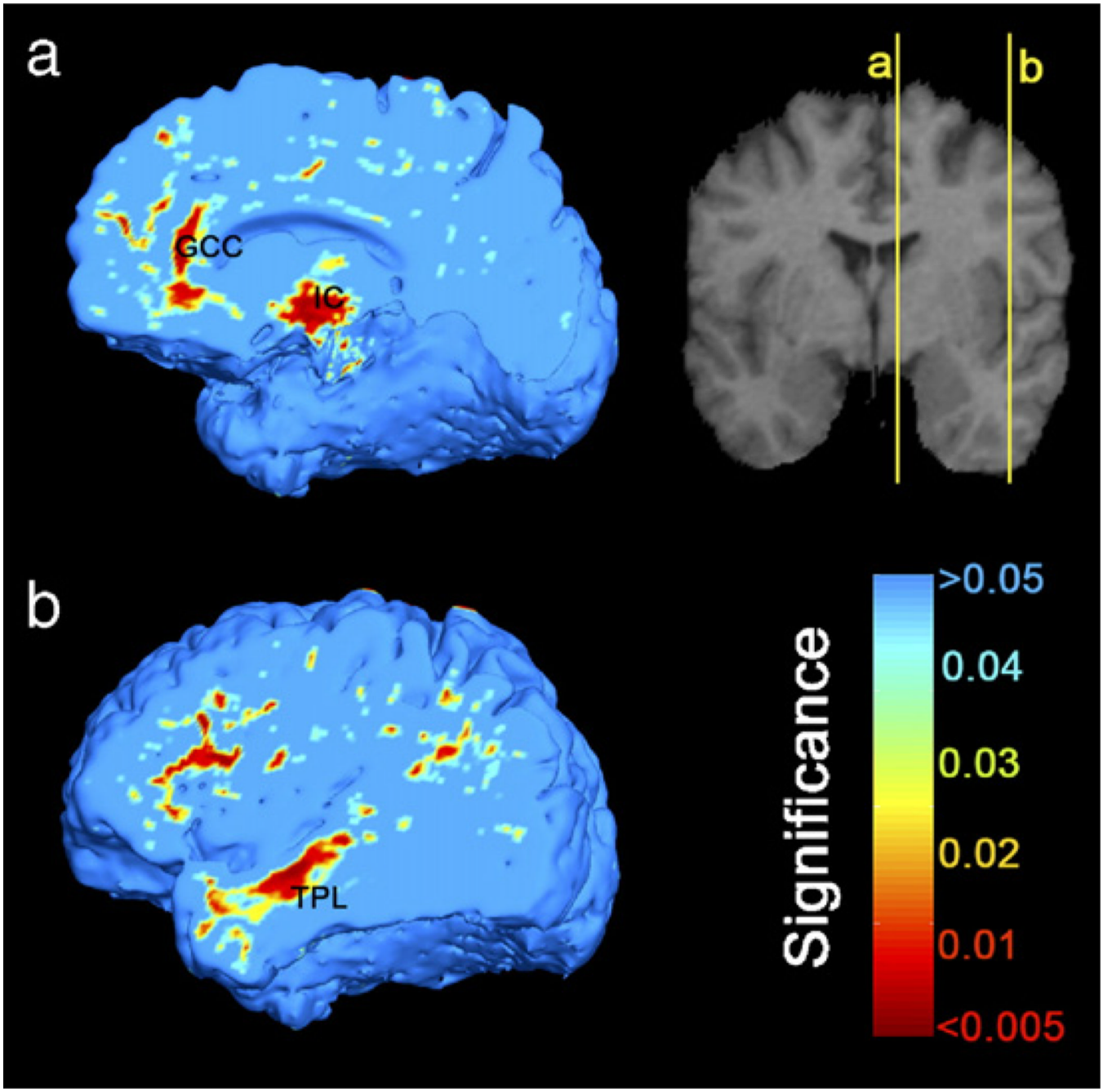

Fig. 10.

In healthy subjects, brain volume decreases with aging in (a) the genu of corpus callosum (GCC), posterior limbs of internal capsule (IC) bordering on the ventrolateral thalamus, (b) anterior frontal, and lateral temporal lobes (TPL). On the other hand, such linkage was not detected in AIDS patients (maps not shown), nor was a disease × age interaction, perhaps due to small sample sizes and the relatively restricted age range.